49

Observations of ribbing instabilities in elastic fluid flows with gravity stabilization

By ANNE M. GRILLET, ALEX G. LEE
AND ERIC S. G. SHAQFEH

Department of Chemical Engineering, Stanford University, Stanford, CA 94305-5025, USA

We have investigated the role of elasticity in the stability of air–fluid interfaces during fluid displacement flows. Our investigations of the stability of coating flows with an eccentric cylinder geometry for both a viscous Newtonian fluid and ideal elastic Boger fluids are discussed in terms of three classes of phenomena. To begin, we have documented several new features in traditional fingering instabilities in elastic displacement flows. These include a very strong elastic destabilization of forward roll coating: a destabilization which can be correlated directly with the elasticity of the coating fluid and which appears to be present even in the absence of diverging channel walls. Moreover, elastic effects are shown to create a novel saw-toothed cusped pattern in the eccentric cylinder roll-and-plate geometry. Secondly, we have found that purely elastic bulk flow instabilities in the neighbourhood of air–fluid interfaces can cause surface deformations if the secondary flow is of sufficient strength. Finally, flows created by the displacement of less viscous air by a more viscous elastic fluid are found to display a new class of purely elastic instabilities which appear to be independent of traditional viscous fingering instabilities and elastic bulk flow instabilities. Thus interfaces which are stable for Newtonian fluids are unstable via purely elastic mechanisms. We have found that indeed elasticity has a dramatic effect on the stability of interfaces, not only changing the critical conditions, but also changing the manifestation of traditional fingering instabilities, and causing new purely elastic interfacial instabilities.

1. Introduction

Coating a uniform thin film onto a substrate is very important in the production of such household items as photographic film and paper (Ruschak 1985). Interfacial viscous fingering or ribbing instabilities can lead to uneven coatings and limit the processing speeds of coating applications (Strenger, Secor & Lenx 1997). The understanding of coating processes is hampered by the complexity of the two-dimensional flows and, in this context, there have been a wide variety of geometries which have been studied, including blade coaters, extrusion slot coaters, forward roll coaters (co- and counter-rotating), and roll–plate coaters (Ruschak 1985). There has been a large body of work focused on the coating of Newtonian fluids (in all the geometries mentioned above) in an effort to better understand and thereby prevent interfacial instabilities in industrial processes (Pearson 1959; Pitts & Greiller 1961; Mill & South 1967; Greener *et al.* 1979; Sullivan & Middleman 1979; Rabaud, Michalland & Couder 1990; Coyle, Macosko & Scriven 1990). Despite the fact that many industrial coating processes involve polymeric fluids, the role of elasticity in the development

of the base flows and their stability is not well understood (Ning, Tsai & Lui 1996; Soules, Fernando & Glass 1988; Bauman, Sullivan & Middleman 1982; Dontula *et al.* 1996; Strenger *et al.* 1997).

Recently there has been much progress in the understanding of the rheology of dilute polymer solutions and the mechanisms whereby polymeric stresses can cause flow instabilities. An example is the discovery and stability analysis of the purely elastic Taylor–Couette instability by Muller, Larson & Shaqfeh (1989), Larson, Shaqfeh & Muller (1990) and Shaqfeh, Muller & Larson (1992). This elastic Taylor–Couette instability occurs in the limit of creeping or Stokes flow where inertial effects are negligible. Thus, it is caused solely by the presence of polymers and hence elastic stresses in the flow. In the analysis by Larson *et al.* (1990), the critical conditions were found to depend on the parameter $\epsilon^{1/2} Wi$ where $Wi = \lambda \times$ wall velocity/gap width is the Weissenberg number, representing the ratio of elastic to viscous forces in the flow; λ is the relaxation time of the fluid and ϵ is a geometric parameter defining the dimensionless curvature in the flow. For Taylor–Couette flow ϵ equals the gap width divided by radius of the cylinder. Similar purely elastic instabilities have been studied in several other geometries including Taylor–Dean flow (Joo & Shaqfeh 1991, 1994), eccentric cylinder flow (Dris & Shaqfeh 1995), cone-and-plate and plate-and-plate flows (Magda & Larson 1988; Byars *et al.* 1994) and others as summarized in a recent review article by Shaqfeh (1996). Recirculation flows, specifically cavity flows (McKinley, Pakdel & Öztekin 1996) and block flows (Joo 1993; Grillet & Shaqfeh 1996), where the radius of curvature of the streamlines is comparable to the cavity dimension, also exhibit elastic instabilities. Elastic instabilities in these flows are of particular interest since most coating and fluid displacement flows are characterized by fluid recirculation regions or other regions of curved streamlines (Aidun, Triantafillopoulos & Benson 1991; Sullivan & Middleman 1979; Fernando & Glass 1988). Despite the differences in geometries, most of the instabilities mentioned above appear to occur at a critical value of the same dimensionless parameter, $\epsilon^{1/2} Wi$, introduced for Taylor–Couette flow (Muller *et al.* 1989; Larson *et al.* 1990; Shaqfeh *et al.* 1992; Joo & Shaqfeh 1991, 1994; Dris & Shaqfeh 1995; Byars *et al.* 1994; McKinley *et al.* 1996) – where ϵ is a geometric ratio given as the characteristic scale of the shear to the (local) radius of curvature of the flow. McKinley *et al.* (1996) showed that for cavity flows, ϵ is dependent on the aspect ratio AR through the relationship $\epsilon = (a + b/AR)$, where a and b are constants. To date, there have been three primary mechanisms proposed for purely elastic shear flow instabilities, all of which depend on the occurrence of hoop stresses created by the stretching of polymer molecules around curved streamlines (Shaqfeh 1996). An understanding of these mechanisms is potentially useful in identifying flows which are susceptible to elastic instabilities.

Viscous fingering instabilities of Newtonian fluids in Hele–Shaw and porous media flows, as described in a recent review article by Homsy (1987), are driven, in general, by differences in the pressure gradient between two fluids in fluid–fluid displacement flows. If the displacing fluid is less viscous than the displaced fluid (which is the case for most coating flows), the interface may be unstable for all velocities. If the displacing fluid is more viscous, then the interface is generally stable, though recently Michalland, Rabaud & Couder (1996) have shown that there are some exceptions for flows of Newtonian fluids between converging walls. Our experiments are not within the small unstable regime they found, so for the following discussion, flow with a more viscous Newtonian displacing fluid is stable. We shall denote these two classes of coating flows air⇒fluid displacement and fluid⇒air displacement flows respectively.

If the Hele–Shaw cell is aligned vertically and if the less viscous upper fluid is displacing a denser fluid below, then gravity will in general stabilize the advancing interface. The stability analysis to determine the onset condition for fingering was accomplished in an early analysis by Saffman & Taylor (1958). Their expression gives a critical condition for air⇒fluid displacement in terms of the dimensionless capillary number, the ratio of viscous to surface tension forces, as

$$Ca_{crit} = \frac{\mu U}{\sigma} = \frac{(\rho - \rho_{air})gb^2}{12\sigma} \tag{1.1}$$

where μ is the fluid viscosity, U the mean flow velocity, σ the surface tension, ρ is the fluid density, ρ_{air} is the air density, g is the gravitational acceleration constant, and b is the gap thickness. Alternatively, we can write this condition as

$$\frac{Ca}{Bo} = \frac{\mu U}{\rho g b^2} = G = \frac{1}{12} \tag{1.2}$$

where the ratio of capillary to Bond numbers is written as G the gravity parameter. This dimensionless parameter relates the strength of the viscous forces to gravitational forces. For sufficiently small gaps, the gravity effects are small relative to surface tension (Coyle *et al.* 1990) since the associated Bond number $Bo = \rho g b^2/\sigma$ is small.

If the bounding walls of the Hele–Shaw cell are not parallel then the diverging or converging walls can effect the critical condition for fingering instabilities in Newtonian fluids as shown by Pearson (1959) and Pitts & Greiller (1961). They found that if a more viscous fluid was driven from a diverging channel (figure 1*a*), then the interface would be stable below a critical speed which was dependent on the divergence angle α or wall slope $\tan(\alpha/2)$. Likewise displacement from a converging channel was destabilized relative to that between parallel walls. For a given diverging channel, Pitts & Greiller (1961) completed a one-dimensional stability analysis in the absence of gravitational effects and found the critical condition to be

$$Ca_{crit} = \tfrac{1}{3}\tan(\alpha/2). \tag{1.3}$$

Despite the explicit role of the divergence angle, researchers have in general presented their results in terms of the dimensionless minimum gap width (Pitts & Greiller 1961; Mill & South 1967; Greener *et al.* 1980; deBruyn & Pan 1995), because the gap width is a fixed geometric parameter in experiments. On the other hand, the divergence angle is difficult to measure experimentally, since it is a function of the location of the meniscus which is in turn a complex function of the two-dimensional flow. As a result a number of researchers have found different power-law scalings for the dependence of the critical capillary numbers on the dimensionless gap width. Coyle *et al.* (1990) were able to explain these scaling discrepancies in the experimental results on forward roll coating by using finite element simulations to model the two-dimensional flow (shown in figure 8 versus wall slope $\tan(\alpha/2)$). Their stability analysis compared well with experimental data over two orders of magnitude of dimensionless gap widths.

Although the critical conditions for fingering in Newtonian fluids are well understood, the effects of fluid elasticity on these conditions are less clear. Fingering instabilities in radial Hele–Shaw cells with Boger fluids and shear–thinning polyacrylamide fluids have been experimentally investigated by Allen & Boger (1988) and Weisser (1996). For immiscible fluids, Allen & Boger (1988) found that the fingering patterns for these highly elastic fluids and Newtonian fluids were remarkably similar for comparable viscosity ratios. While they did not calculate a Weissenberg number for their flows, they postulated that the Weissenberg number in their experiments may
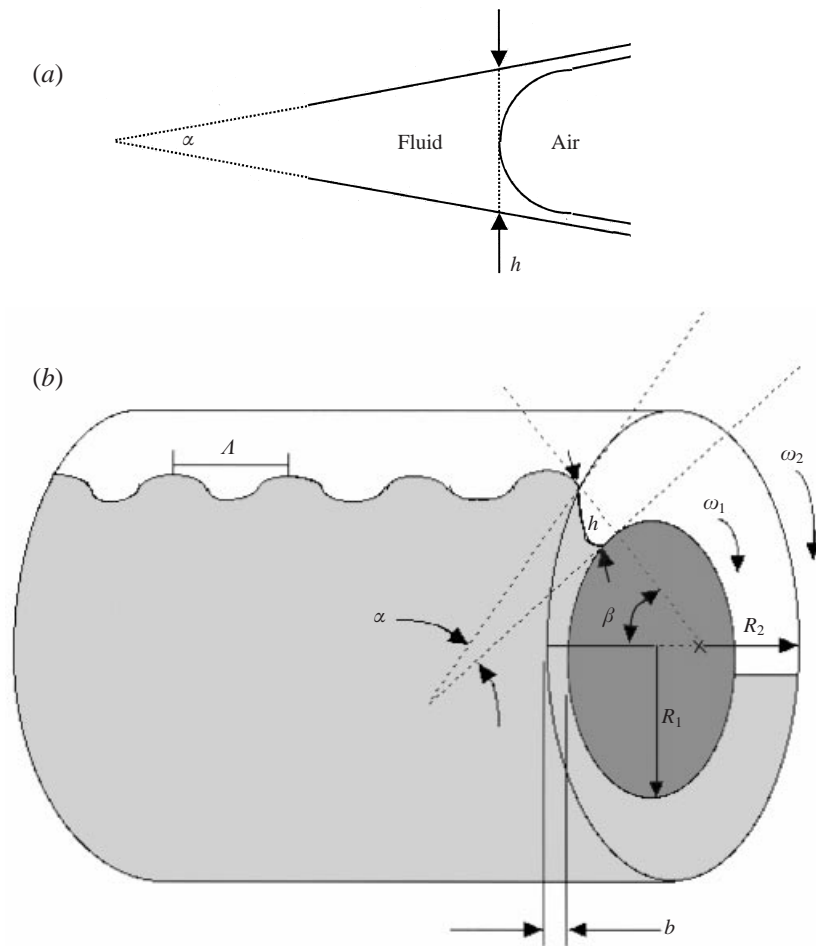
FIGURE 1. Experimental geometries: (*a*) diverging wedge;
(*b*) eccentric cylinder coating apparatus.

have been too low to witness a significant elastic effect. Weisser (1996) investigated the radial Hele–Shaw cell with miscible fluids and also found no significant elastic effect. Both researchers did find that shear-thinning fluids displayed much finer fingering patterns.

The stability of polyacrylamide Boger fluids in the forward roll coating and roll–plate geometries has been investigated by Bauman *et al.* (1982) and later by Dontula *et al.* (1996). Even for a fluid with a concentration of 10 p.p.m. of polymer which exhibited no measurable normal forces under shear, the critical conditions for the instability decreased by a factor of two. A qualitative explanation of the destabilizing effect of the polymer additive was developed by looking at the local extensional flow near the stagnation point on the free surface; however there was no quantitative comparison between theory and experiment. The importance of the extensional behaviour of polymeric fluids to coating instabilities was studied by Soules *et al.* (1988). Using a spinning fibre apparatus to measure the dynamic uniaxial extensional viscosities of many polymer coating fluids, they found that increased extensional viscosities decreased the critical capillary number for fingering instabilities in a forward roll

coating device. On the other hand, elasticity was found to be stabilizing in extrusion slot coating (Ning *et al.* 1996).

This paper continues an ongoing investigation of purely elastic instabilities in recirculation flows, focusing on recirculation flows with free surfaces. We began our study by looking at purely elastic bulk flow instabilities in the neighbourhood of a free surface, though we quickly expanded the scope as we discovered rich and diverse dynamics, with new transitions and a new class of purely elastic interfacial instabilities. To begin, we describe how elasticity can affect traditional viscous fingering in two common air$\Rightarrow$fluid displacement flows. Thereafter we discuss surface deformations caused by purely elastic bulk flow instabilities. Finally, a new class of purely elastic interfacial instabilities in fluid$\Rightarrow$air displacement flows will be examined. As an introduction to these investigations, we next describe our experimental apparatus.

2. Experimental apparatus

In our experiments, air$\Rightarrow$fluid and fluid$\Rightarrow$air displacement flows are created by placing one cylinder inside another and filling the gap between the cylinders half full of liquid (figure 1*b*). The outer cylinder, which has a radius of $R_2 = 8.5$ cm, is machined and polished Plexiglas to allow complete visualization of the interface. The inner cylinder is anodized aluminium with a radius of $R_1 = 7.5$ cm. The surface roughness of both cylinders was measured to be less than $10 \, \mu$m which should not be significant since our minimum gaps widths are $\geqslant 1000 \, \mu$m $= 1$ mm. The angular velocity (ω_1, ω_2) of each cylinder is independently computer controlled (Joo & Shaqfeh 1994). The axis of the inner cylinder can be shifted parallel to the axis of the outer cylinder such that eccentric cylinder flow can be generated. The minimum gap in all geometries is denoted as b and ranged from 1 mm to $b_{max} = 1$ cm (i.e. concentric cylinder flow). One endwall (left side of figures 10, 12 and 15) is held stationary while the other endwall rotates with the outer cylinder. For experiments with only one cylinder rotating, we have always used the inner cylinder to remove the asymmetric end conditions. The Reynolds numbers are < 0.05 for all flows examined, and therefore in later discussions we will always exclude inertial effects.

This experimental system allows us great flexibility in that we can study diverging and parallel channels in the neighbourhood of the air–liquid interface simply by adjusting the eccentricity of the cylinders. Besides eccentricity, we can also modify the flow by placing a block between the two cylinders which is mounted on the stationary endwall. A Teflon sheath around the block presses against and seals the cylinder walls preventing fluid flux in the azimuthal direction. This block thus introduces a pressure gradient opposing the shearing motion in the fluid. The block is designed such that it can only be used in the concentric cylinder configuration.

Eccentric and concentric cylinder geometries have also been used to study purely elastic instabilities in the bulk (i.e. in the absence of fluid–air interfaces) (Muller *et al.* 1989; Joo & Shaqfeh 1991; Dris & Shaqfeh 1995). The critical conditions for these instabilities (in the geometry of our experiments) are all above $Wi = \lambda \dot{\gamma} \geqslant 15$ where λ is the relaxation time of the fluid and $\dot{\gamma}$, the ratio of average wall velocity and gap width, is a characteristic shear rate. These critical values are well above the relevant critical Wi for the work presented in this paper (Dris & Shaqfeh 1995; Joo & Shaqfeh 1994). On the other hand, the recirculation region near the block displays purely elastic instabilities at lower critical values, $Wi_c = 2$–4 (Grillet & Shaqfeh 1996). Thus these blocked geometries provide an opportunity to investigate the effect of purely elastic bulk flow instabilities on nearby interfaces.
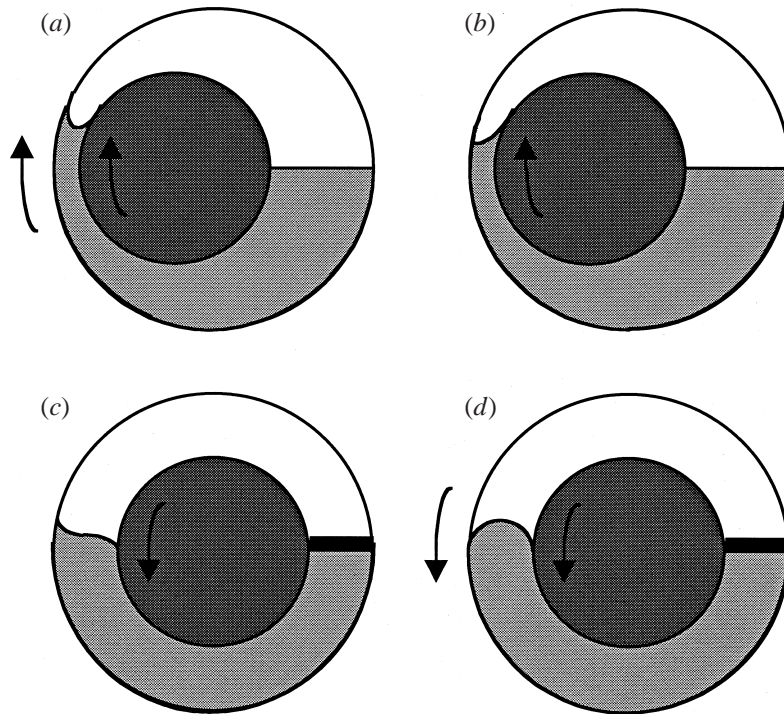
FIGURE 2. Coating and injection flows studied: (*a*) eccentric cylinder forward roll coating flow; (*b*) eccentric cylinder roll-and-plate flow; (*c*) inverse roll-and-plate flow; (*d*) inverse forward roll coating flow.

This paper will focus on four flows which we found to display the most interesting dynamics (figure 2). First we look at eccentric cylinder forward roll coating flow where both cylinders are co-rotating at the same angular speed towards the air ω: this is denoted as (*a*) in figure 2. Since the difference in the radii of the two cylinders is small, the difference in the linear speeds is neglected and $U = \omega R$ is defined as the average wall velocity where $R = \frac{1}{2}(R_1 + R_2)$ is the average cylinder radius. This flow is analogous to forward roll coating with the associated classical viscous fingering instability (Coyle *et al.* 1990). Second, we investigate the eccentric cylinder coating flow with only one cylinder moving toward the air (*b*): this is similar to the roll-and-plate flow studied by Bauman *et al.* (1982). In this case, the capillary number is defined using only the angular speed of the moving cylinder $U = \omega_1 R$. In both air$\Rightarrow$fluid displacement flows, the fluid leaves a wet film on the surface of the cylinders. Next we examine two fluid$\Rightarrow$air displacement flows where the more viscous fluid is displacing the less viscous air – these flows are stable to traditional Newtonian viscous fingering instabilities. Two cases are studied: (*c*) inverse roll-and-plate flow with one cylinder moving into the fluid at the interface ($U = \omega_1 R$), and (*d*) inverse forward roll coating flow where both cylinders move at the same speed into the fluid ($U = \omega R$). Both of these flows are examined in a concentric cylinder geometry with the Teflon coated block, so the cylinder walls moving into the fluid have traces of fluid (i.e. the fluid has not dewetted from the surface) but the film thicknesses are not measurable.

Some unique aspects of our apparatus should be kept in mind when considering our results. The divergence angle between the two cylinders is small compared to

most forward roll coaters because the divergence is due to the difference in curvature of the cylinders and the cylinders are of similar size. In our experiments the largest divergence angle was around 5°, compared to divergence angles of over 80° achievable in Coyle *et al.* (1990)'s forward roll coating apparatus. The length of the device, L, is 16 cm; so for a minimum gap width of 0.1 cm, the dimensionless length of the coating gap between the cylinders, $L/b = 16 \, \text{cm}/0.1 \, \text{cm} = 160$. DeBruyn & Pan (1995) found finite end effects to be stabilizing for the eccentric cylinder roll–plate flow, thus we anticipate that finite end effects may also influence the onset of the instability in our experiments. However, they found that sufficiently above the critical condition, there was no difference in the measured wavelength compared to an 'infinite' cylinder experiment. Another important factor in our experiments is that gravity is a significant and usually the dominant stabilizing agent because of the relatively large gap sizes used. Thus $\rho g b^2 / 12\sigma$ (cf. (1.1)) is comparable to or greater than $\tan(\alpha/2)/3$ (cf. (1.3)) in most of our experiments. Therefore, gravity stabilizes the interface and can also affect the wavelength selection process (Saffman & Taylor 1958).

Determining the critical condition for these interfacial instabilities can be difficult. Unaided visual observation of the interface for deformations may appear rather arbitrary, but in a comparison of three decades of visual observation data of forward roll coaters, Coyle *et al.* (1990) found that all of the data coincided very well. The critical condition in our experiments was determined when deformations were visible at the interface which were sinusoidal and distinguishable from small deformations near the ends.

The observed wavelength, $\varLambda$, of the instability was measured by averaging over all of the peaks visible on the interface. For steady interface patterns, the peaks were generally very regular except just at the critical onset of the instability. For more dynamic interface patterns, the peaks were not always as evenly spaced, but in almost all cases the averaged wavelength was constant in time. The wavelength will be reported in terms of the dimensionless wavenumber n defined as

$$n = \frac{2\pi b}{\varLambda}, \tag{2.1}$$

where b is the minimum gap between the cylinders. The observed wavelength can be analysed further by performing a discrete fast Fourier transform on the interface pattern to determine the frequency spectrum of the instability. An image of the unstable interface was captured, digitized and imported into NIH image. 256 points were evenly spaced along the the unstable interface and the vertical position of the interface was recorded. The mean interface location was subtracted from the points to remove the delta function at zero in the intensity spectrum and the dominant wavenumber of the resulting spectrum is defined as the n_{FFT}. We will show that the results are consistent with the observed wavenumber for cases where the unstable interface is stationary in time.

Two types of fluid were used in this study: the Newtonian fluid was an Amoco H–40 Indopol polybutene polymer with number averaged molecular weight near 750 and a viscosity of 110 P graciously donated by Amoco Chemical Company. The viscoelastic Boger fluids were made by mixing 0.1 wt% high molecular weight polyisobutylene (Scientific Polymer Products, Inc$-M_n = 4,700,000$) into a combination of 3.5 wt% kerosene (Aldrich) and 96.4 wt% polybutene (Amoco Chemical Co.). The viscosity of the final solution was controlled through the polybutene solvent viscosity by combining the H–40 Indopol product with H–100 Indopol polybutene ($M_n = 940$, $\mu \approx 215$ P). These fluids were characterized using a Rheometrics Dynamic Analyzer II
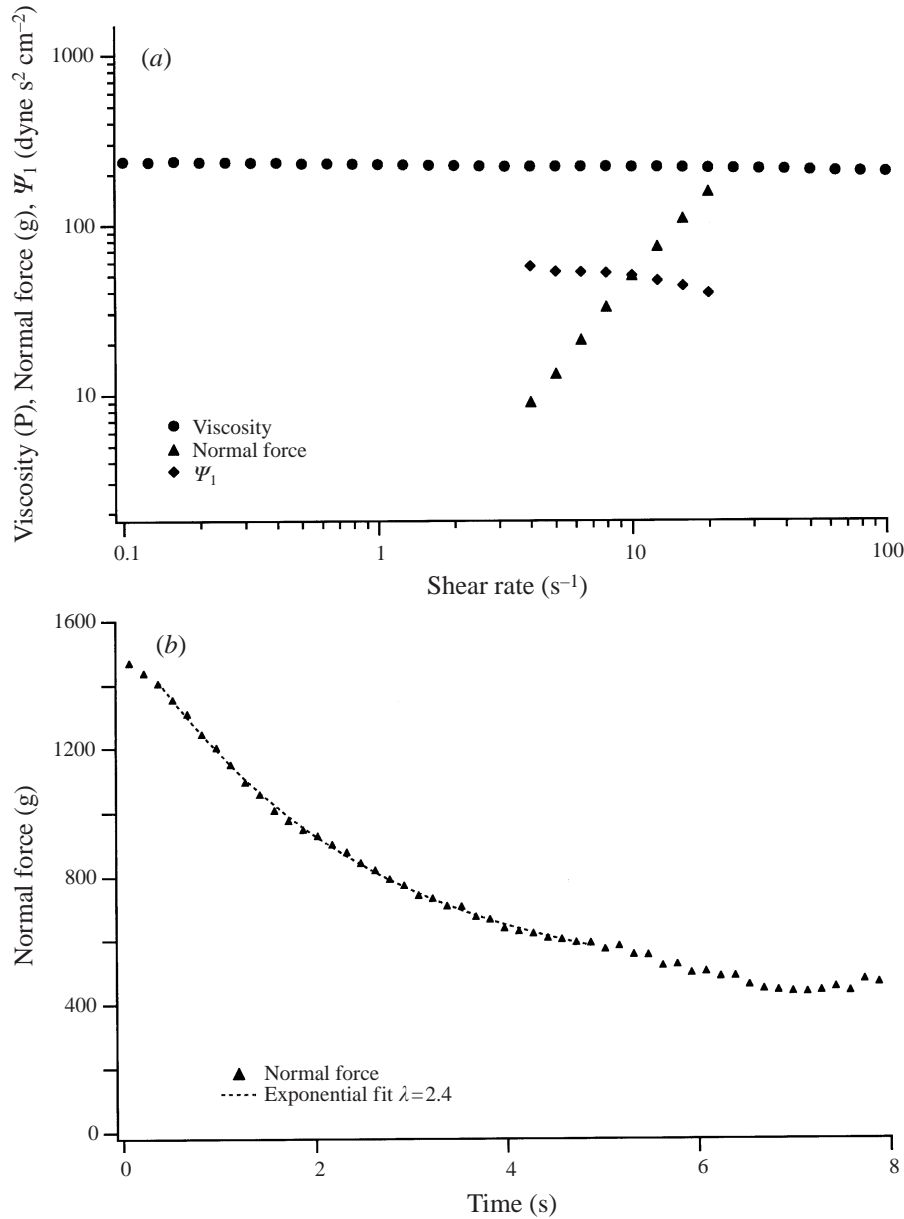
FIGURE 3. Typical rheology of experimental Boger fluids: (*a*) steady shear rate sweep;
(*b*) normal force decay after cessation of steady shear and exponential fit.

normal stress, controlled strain rheometer. The pure polybutene exhibited a constant shear viscosity and no measurable normal force over a wide range of shear rates (0.1–$50\,\mathrm{s}^{-1}$). The first normal stress coefficient, Ψ_1, for the viscoelastic fluid was approximately constant over a decade of shear rates (3–$20\,\mathrm{s}^{-1}$) and the shear viscosity was constant over three decades (figure 3*a*), as is usually characteristic of ideal elastic fluids (Boger & Mackay 1991; Larson 1988). The relaxation times of the elastic fluids, λ, were determined by fitting the decay of the normal stress after steady shear to a single exponential (figure 3*b*). While this is only an approximation of the spectrum of

$\mathcal{N} = \dfrac{\lambda\sigma}{\mu b_{max}}$	μ (P)	λ (s)	σ (dyne cm^{-1})
Newtonian	96	0.0	29.4
0.19	326	2.1	30.0
0.47	217	3.2	32.0
0.62	234	4.4	32.8
0.96	117	3.5	32.0

TABLE 1. Physical properties for experimental fluids.

relaxation times possessed by a real fluid, this transient relaxation time has been found to correlate the occurrence of purely elastic instabilities (Larson *et al.* 1990; Magda & Larson 1988). These tests were performed for the range of temperatures used in our experiments (19–21 °C), so the temperature dependence of the viscosity and relaxation times was taken into account when calculating the Weissenberg and capillary numbers for each experiment. Surface tension was measured using a Wilhelmy balance for several temperatures and found to be relatively insensitive to temperature variation. To get a measure of the elasticity of each of the Boger fluids which is not dependent on the velocity or experimental gap width, we define an elasticity parameter $\mathcal{N}$ as the ratio of the Weissenberg and capillary numbers at the maximum gap width:

$$\mathcal{N} = \frac{U\lambda/b_{max}}{\mu U/\sigma} = \frac{\lambda\sigma}{\mu b_{max}}. \tag{2.2}$$

Note that $\mathcal{N}$ is defined using the gap width in concentric cylinders $b_{max} = 1\,\text{cm}$, so that the $\mathcal{N}$ value for a given fluid is independent of the minimum gap width b and therefore is a constant for a series of experiments at varying gap widths. Physically this parameter can be thought of as the ratio of the polymer relaxation time and the time for an interface deformed by an amount b_{max} to relax under surface tension. The fluids used in these experiments spanned $\mathcal{N}$ values from zero to one. Table 1 presents the physical properties for most of the fluids used in this work listed by their $\mathcal{N}$ values.

These fluids were seeded with $< 0.01\,\text{wt\%}$ mica flakes (Mearl Corp.) in order to visualize any secondary flow. Pakdel, Speigelberg & McKinley (1997) have shown that the addition of mica flakes to a similar Boger fluid does not measurably change the rheology. An instability in the bulk fluid is manifested by light and dark striped bands as the small particles align with the vortices of the secondary flow. For a global instability such as the purely elastic Taylor–Couette instability, the pattern appears in all of the fluid when the critical Weissenberg number is reached (Muller *et al.* 1989). For local instabilities, such as the recirculation block instability, the banded mica pattern appears locally in the unstable recirculation region at the critical condition, then propagates into the bulk fluid as the velocity is increased further (Grillet & Shaqfeh 1996). This indicates that the secondary flow created by the instabilities is advecting downstream.

3. Eccentric cylinder forward roll coating flow

We shall begin our discussion of the effect of elasticity on the stability of interfaces in air⇒fluid displacement flows by presenting our results on the eccentric forward roll coating flow (figure 2*a*). This flow has been the most widely studied by previous
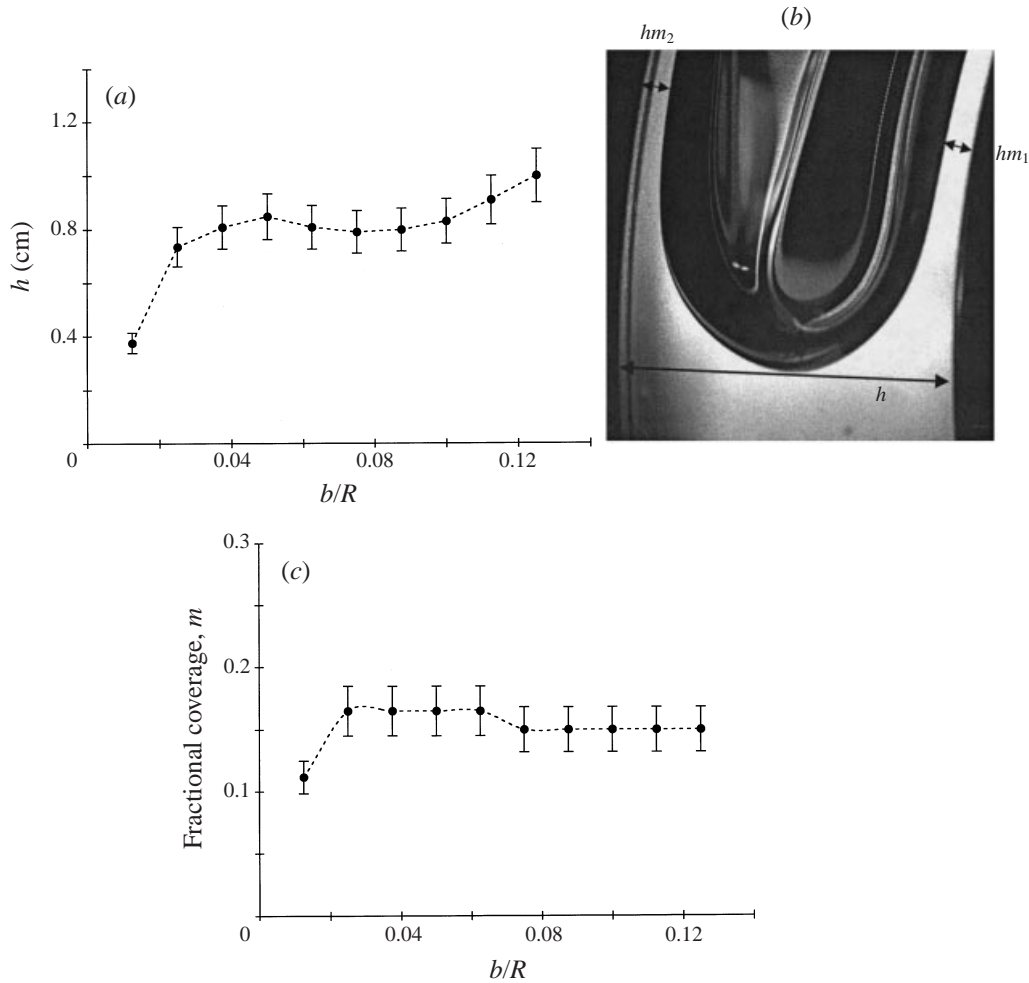
FIGURE 4. Experimental measurements of gap width at the interface and coating film thickness on cylinder walls: (*a*) measurements of h the gap width at the meniscus; (*b*) sample digital image of coating films; (*c*) measurements of the coating film thickness $m_1 = m_2 = m$ for the Newtonian fluid (- -●- -).

researchers (Coyle *et al.* 1990), and is one of the few such flows which has been investigated with elastic fluids (Soules *et al.* 1988; Bauman *et al.* 1982; Dontula *et al.* 1996; Fernando & Glass 1988). In addition, there are explicit theoretical predictions for the dispersion relationship and critical conditions for Newtonian fluids (Saffman & Taylor 1958). Thus, by comparison with all of these results, we seek to understand the effect of elasticity on the critical capillary number.

We first report on an investigation of the stability of Newtonian fluids for a range of dimensionless minimum gap ratios, b/R. For capillary numbers at which the flow is stable, the interface remained smooth, producing an even coating on the surfaces of the cylinders. The angular location of the interface on the outer cylinder, β, was recorded and used to calculate the local divergence angle of the cylinder walls, α, as well as the local gap thickness at the meniscus, h (figure 4*a*). We can also experimentally measure the thickness of the fluid film while the flow is stable by digitally photographing a radial slice illuminated with a laser sheet (figure 4*b*).

Figure 4(*b*) shows the thickness of an individual Newtonian film where the fractional coverage of a film at the meniscus is defined as

$$m_1 = \frac{\text{film thickness on inner cylinder}}{h}, \tag{3.1}$$

$$m_2 = \frac{\text{film thickness on outer cylinder}}{h}. \tag{3.2}$$

The inner and outer film thicknesses were found to be comparable ($m_1 \sim m_2 = m$ in figure 4*c*) and the fractional coverage m was found to remain fairly constant for $b/R > 0.025$.

Above a critical capillary number, undulations appeared in the interface which thereafter grew in amplitude to form fingers. These critical conditions are plotted versus the gap ratio and compared to a modified Saffman–Taylor theory for Newtonian fluids (figure 5). This modified Saffman–Taylor theory includes the gravity stabilization and the stabilization due to the gap divergence. However it includes the latter only through a one-dimensional analysis originally presented by Pitts & Greiller (1961) and does not include the global two-dimensional flow effects (i.e. the streamwise variation of the lubrication flow) which is necessary to properly characterize the long waves (Pearson 1959; Reinelt 1995). We shall return to these shortcomings below. The modified Saffman–Taylor theory can be summarized by the set of equations

$$\Gamma = Ca\,\tilde{n} - \frac{\tilde{n}Bo\,h^2\cos(\beta)}{12b^2} - \frac{\tilde{n}\tan(\alpha/2)}{3} - \frac{\tilde{n}^3}{12}, \tag{3.3}$$

$$Ca_{crit} = \frac{\tan(\alpha/2)}{3} + \frac{Bo\,h^2\cos(\beta)}{12b^2}, \tag{3.4}$$

$$G_{crit} = Ca_{crit}/Bo, \tag{3.5}$$

$$\tilde{n} = 2\pi h/\Lambda, \tag{3.6}$$

where $\tilde{n}$ is the dimensionless wavenumber of the disturbance scaled with the gap width at the meniscus. The Bond number Bo and the gravity parameter G are defined in terms of the important dimensional parameters as

$$Bo = \frac{\rho g b^2}{\sigma}, \quad G = \frac{\mu U}{\rho g b^2}. \tag{3.7}$$

Moreover, Γ is the growth rate of the surface deformations (made dimensionless with $\sigma/\mu R$). On the right-hand side of (3.3), the last two terms are clearly stabilizing (as is the gravity term proportional to Bo) and are due to surface tension. The term proportional to $\tan(\alpha/2)$ is the stabilization due to the channel divergence. As discussed in the Introduction, we found that over the entire range of dimensional gaps examined ($1\,\text{mm} \leqslant h \leqslant 1\,\text{cm}$) the gravitation stabilization was comparable to or greater than that due to surface tension. This was actually tested in two different ways. First we calculated the ratio of the gravity stabilization term (term 2 on the right-hand side of (3.3) above) to the surface tension stabilization terms (terms 3 and 4 on the right-hand side of (3.3) and found that above a dimensionless gap of $b/R \approx 0.009$ the former was dominant. Secondly, we rotated our apparatus 90° counterclockwise from the configuration shown in figure 2(*a*) such that gravity was acting normal to the cylinder walls at the minimum gap and found that the critical conditions for onset of fingering departed from and fell significantly below those reported in figure 5 for gaps greater than $b/R \approx 0.009$. Thus we have chosen to present our results (figure 5*a*) in terms
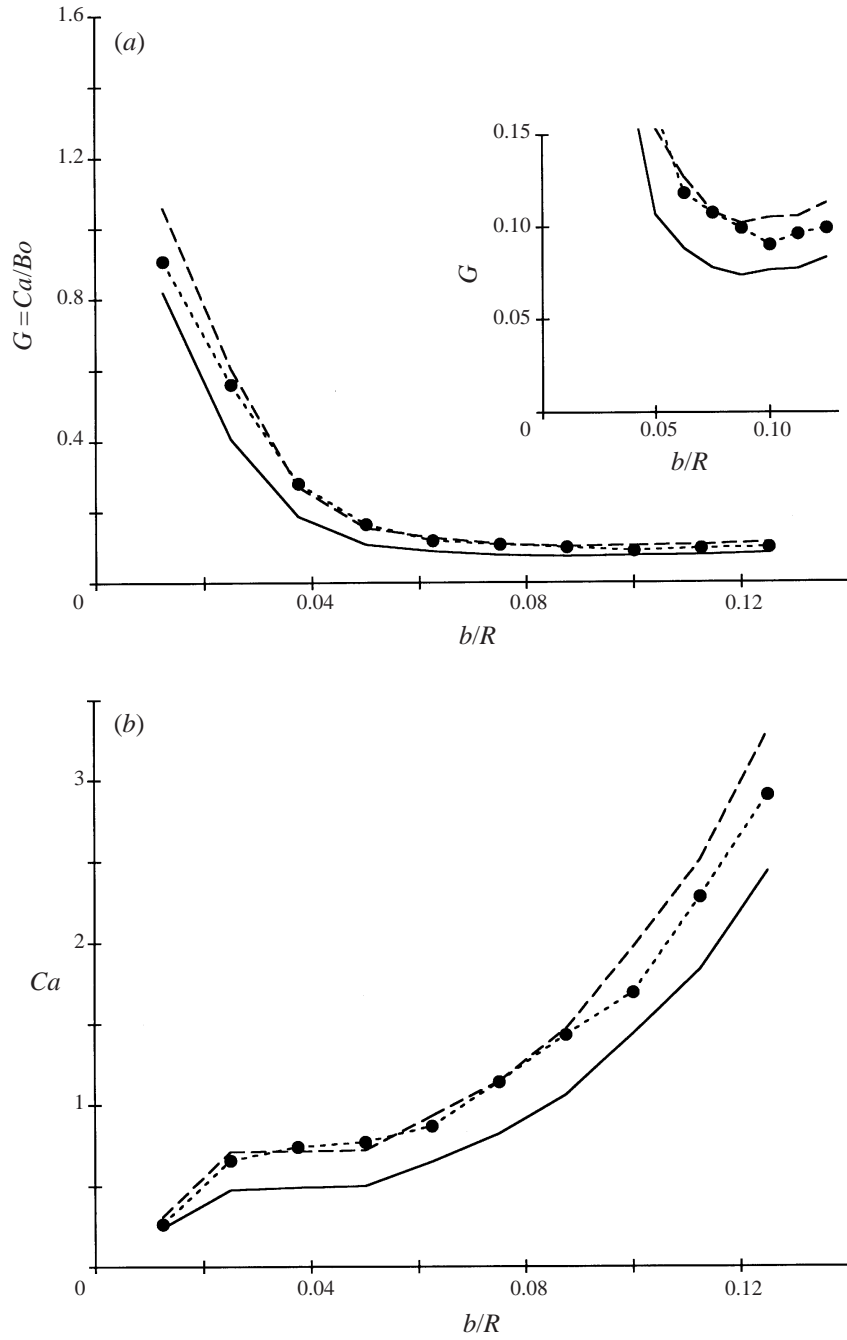
FIGURE 5. Comparison of the critical condition versus the dimensionless gap ratio from the experimental measurements for a Newtonian fluid (- -●- -), the modified Saffman–Taylor theory (——) and new theory for gravity-stabilized viscous fingering which includes film thickness (– – –): (*a*) gravity parameter; (*b*) capillary number.

of the gravity parameter, G, where appropriate. Since the location of the interface β, and hence the gap width at the meniscus h, are not known *a priori*, these values are determined from experiment and used to calculate the predicted critical condition for each geometry. Note that the agreement is fairly good over the entire range with the measured critical conditions being about 5–10% above the Saffman–Taylor theory throughout. To expand the data for large gaps where the data are almost overlapping, we have also included a small inset plot. For the smallest gap studied, $b/R = 0.0125$, the critical linear speed of the cylinders for a Newtonian fluid was $U = 0.08\,\mathrm{cm\,s^{-1}}$, while for the concentric case, the critical speed increased to $U = 0.94\,\mathrm{cm\,s^{-1}}$. We should note that the applied acceleration rate $5\,\mathrm{cm\,s^{-2}}$ is quite large so the speed reaches a constant value within seconds, whereas the onset of the instability at critical usually takes more than 5 minutes.

The uniform 5–10% discrepancy from the Saffman–Taylor result is significant however and some discussion is appropriate (we note in this context, that when presented in terms of the critical capillary number, cf. figure 5*b*, the error is somewhat larger). From the Saffman–Taylor result (3.3) the instability is a long-wave instability, but it has been recognized previously by Pearson (1959), Pitts & Greiller (1961) and in calculations by Reinelt (1995) for the eccentric cylinder geometry that global effects, i.e. those on the streamwise long length scale of the lubrication flow, determine the stability of waves which are of comparable dimension to the streamwise scale. In the eccentric cylinder device, for small gaps and thus in the surface-tension-dominant regime, calculations by Reinelt (1995) and Pitts & Greiller (1961) showed that the resulting waves were chosen to be of size $(Rb)^{1/2}$ and thus the dimensionless wavenumber is $O(b/R)^{1/2}$. These global effects cause a change in the critical condition for the long waves which is comparable to the square root of the ratio of the gap to cylinder radius (in our experiments about 20%). These global effects are not included in the modified Saffman–Taylor result in (3.3) and have been found to be stabilizing (Pitts & Greiller 1961; Reinelt 1995). For larger gaps (and thus small eccentricities) we know of no analysis which demonstrates how the wavenumber selection process is modified by the streamwise variation (e.g. curvature) of this nearly concentric cylinder flow. Note that in our experiments, the radius of the cylinders is only half the size of the vessel length, thus it seems reasonable that end effects may also affect the stability process. In another context, deBruyn & Pan (1995) have witnessed strong stabilization of ribbing in the eccentric cylinder roll–plate geometry due to the decreases in dimensionless length of the cylinders L/R (by decreasing the radius of the inner cylinder for a constant length) when compared to the finite element predictions for the forward roll coating geometry by Coyle *et al.* (1990). It is therefore reasonable to assume that the global effects of either curvature or the finite length of the vessel might contribute to the discrepancy in the comparison to the modified Saffman–Taylor theory.

Moreover, the thickness of the coating films deposited on the cylinder surfaces has not been included in the aforementioned theory (i.e. (3.3)). In order to account for the discrepancies between our experiment and the modified Saffman–Taylor theory, we have repeated the one-dimensional analysis including the effect of film thickness (following the analysis of Reinelt 1995). This analysis is summarized in the Appendix as are the approximations made in its development. The resulting growth rate in the limit of long waves was found to be

$$\Gamma = \tilde{n}Ca - \frac{\tilde{n}Bo\cos(\beta)h^2}{12(1-2m)b^2}, \tag{3.8}$$
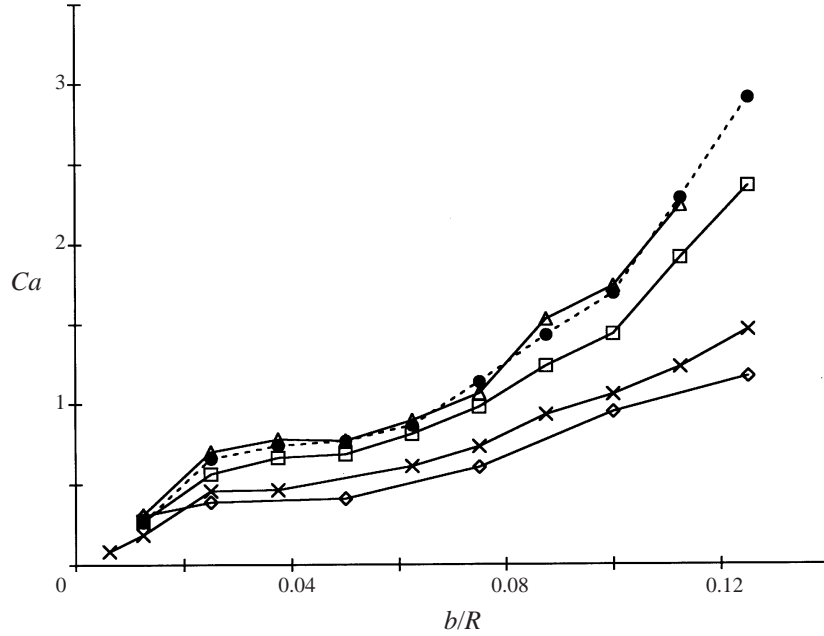
FIGURE 6. Comparison of the critical capillary number in the forward roll coating geometry versus the dimensionless gap ratio from the experimental measurements for a range of fluids: - -●- -, Newtonian fluid. Elastic fluid: —△—, $\mathcal{N} = 0.19$; —□—, $\mathcal{N} = 0.47$; —×—, $\mathcal{N} = 0.62$; —◇—, $\mathcal{N} = 0.96$.

where m is the fluid film thickness coated onto the cylinders. If we set the growth rate to zero, the critical condition is

$$G_{crit} = \frac{\cos(\beta)h^2}{12(1-2m)b^2}. \tag{3.9}$$

The location of the interface and the film thicknesses are measured experimentally and used in (3.9) to calculate the critical condition shown in figure 5. Despite neglecting the stabilization due to both surface tension and the diverging walls, the predictions of this new theory agree with our Newtonian experiments very well. Note that the factor of $(1-2m)$ in (3.9) has the simple physical interpretation that the destabilizing pressure gradient in the base state is reduced by $(1-2m)$ because of the film flow.

Figures 6 and 7 present the critical conditions measured in our eccentric cylinder forward roll coating device for the elastic fluids described in §2 and characterized by elasticity parameters $\mathcal{N} = \lambda\sigma/\mu b_{max} = 0.19, 0.47, 0.62, 0.96$. The data are presented over the same range of gap ratio as for our Newtonian results and the latter are included for comparison. For the weakly elastic fluid, $\mathcal{N} = 0.19$ there is no measurable change in the critical conditions over the Newtonian fluid flow. However for the more elastic fluids, $\mathcal{N} = 0.62$ and 0.96 there is a very significant decrease in the elastic critical speed for the onset of instability causing the critical capillary number to fall by a factor of 3 for the largest gap ratios (i.e. concentric cylinder flow).

The results are again best presented in terms of the gravity number, where the destabilization for these latter two elastic fluids occurs as a near-constant shift of the critical values by nearly a factor of 2 over the entire range of gap ratios. This is clearly evident when we expand the small gravity parameter data in the inset. Whereas the critical gravity parameter was constant at large gaps for the Newtonian fluid, for the
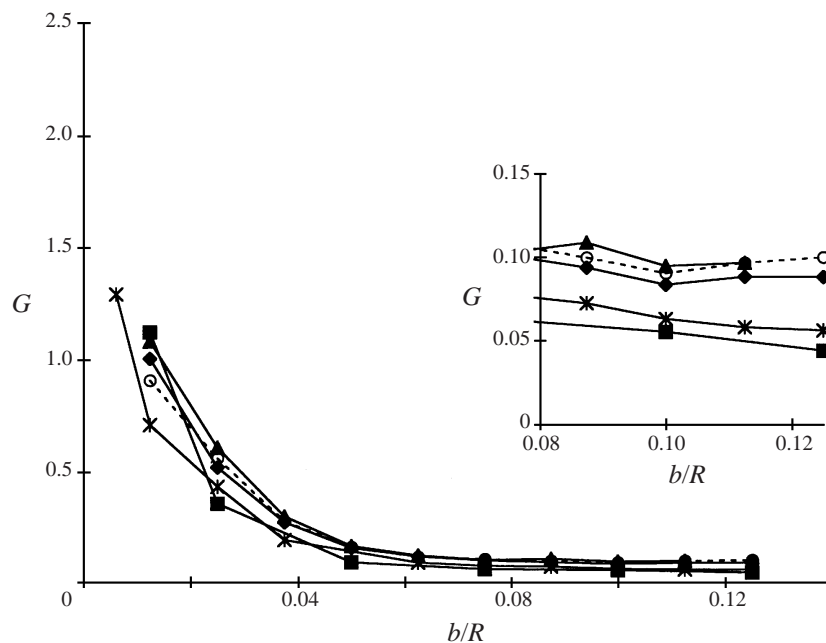
FIGURE 7. Comparison of the critical gravity number versus the dimensionless gap ratio from the experimental measurements for a range of fluids: - -●- -, Newtonian fluid. Elastic fluids: —▲—, $\mathcal{N} = 0.19$; —■—, $\mathcal{N} = 0.47$; —×— , $\mathcal{N} = 0.62$; —◆—, $\mathcal{N} = 0.96$.

elastic fluids the critical condition becomes a strong function of both $\mathcal{N}$ and b/R. We note that there is a large change in the critical conditions between the $\mathcal{N} = 0.47$ and $\mathcal{N} = 0.62$ fluids, and a continued but more modest change when $\mathcal{N}$ is further increased to 0.96.

Our critical capillary numbers are also shown as a function of wall slope $\tan(\alpha/2)$ in figure 8 compared to the Newtonian finite element predictions by Coyle *et al.* (1990) as well as the elastic forward roll coating experiments by Bauman *et al.* (1982) and Dontula *et al.* (1996). Clearly our results are not comparable to any of these theories or measurements primarily because of the gravitational stabilization that is present throughout our experiments (and thus the good agreement with the more complete theory which includes gravity stabilization and film thickness in figure 5). Our experiments at smaller gap widths (the lower portion of our data) approach the other data as the surface tension stabilization becomes comparable to the gravity stabilization in our experiments. Note however that in figure 8 it is demonstrated quite clearly that our critical conditions do not scale with the divergence angle of the channel as would be expected (and is found) if surface tension dominates the stabilization of the fingering pattern. This further confirms our choice of G as the appropriate dimensionless group for our experiments.

The observed dimensionless wavenumber, n, at onset of instability grew approximately linearly for larger gaps ($b/R \geqslant 0.04$) (figure 9). There is significant scatter in the measurements, especially for small wavenumbers since for these cases there were only 1 or 2 wavelengths across the vessel at the critical gravity parameter. This is especially apparent in the Newtonian data where a shift is seen at $b/R > 0.9$ when the instability shifts from two wavelengths at onset to one wavelength. As discussed above, from the calculations by Reinelt (1995) and Pitts & Greiller (1961) we expect that for small
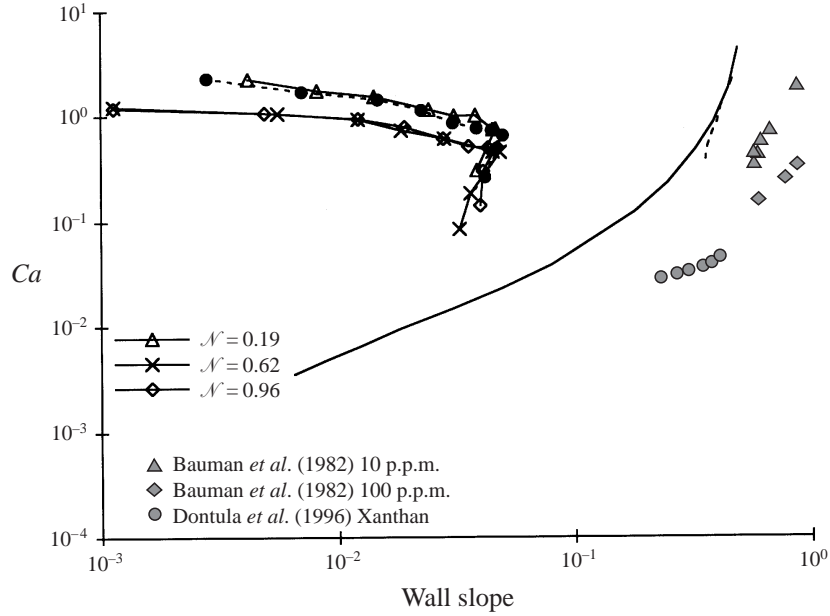
FIGURE 8. Critical capillary number versus wall slope: - -●- -, Newtonian fluid; open symbols, current elastic experiments; ——, Coyle *et al.* (1990) Newtonian simulation; - - - -, Greener *et al.* (1980) Newtonian experiments; grey symbols, previous elastic experiments.

gaps where surface tension is dominant, the dimensionless wavenumber should grow like $(b/R)^{1/2}$ in agreement with the global streamwise variation of the flow stabilizing longer waves. We cannot discern this trend in our experimental data, probably because we have only a small range of very narrow gaps widths where capillary forces are dominant. At large gaps in our experiments, gravitational stabilization is important and as far as we know, no one has considered the wavenumber selection process for Newtonian fluids under these conditions. However, when the same experiments are completed with elastic fluids, a general strong increase in wavenumber at the critical condition was discovered (figure 9). The dimensionless observed wavenumber clearly increased with increasing elasticity and the wavenumbers were as much as a factor of 3–4 higher than those for the Newtonian fluid for the largest gaps and highest values of the elasticity coefficient (figure 9). The trend in the unstable wavenumber with increasing $\mathcal{N}$ is similar to the trend in the critical gravity parameter because the difference in the wavenumber at any value of b/R between the flow at $\mathcal{N} = 0.47$ and 0.62 is larger than the increase caused by further increasing $\mathcal{N}$ to 0.96. Note that for gaps larger than $b/R \geqslant 0.05$ the dimensionless wavenumber $n = 2\pi b/\Lambda$ for both the elastic and Newtonian fingering instabilities increased approximately linearly with gap width, since the measured dimensional wavelength Λ is almost constant for these gap widths. In fact for the highly elastic fluids, within experimental error no increase in critical dimensional wavelength was noted for gap widths greater than $0.02\,R$.

For small gaps, wavenumbers for both elastic and Newtonian flows increased as the wall velocity was increased above the critical condition. The smooth undulating variation in the interface at the critical condition developed into several air fingers separated by liquid bridges and above the critical condition, tip splitting of the air fingers became more frequent. Because of the relatively small divergence angles in our
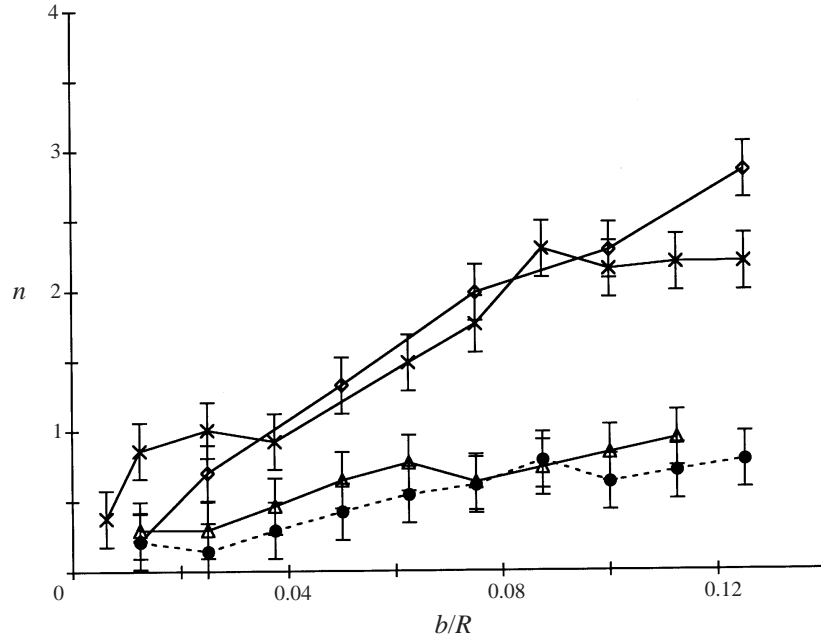
FIGURE 9. Critical wavenumber versus dimensionless gap ratio: - -●- -, Newtonian fluid. Elastic fluids: —△—, $\mathcal{N} = 0.19$; —□—, $\mathcal{N} = 0.47$; —×—, $\mathcal{N} = 0.62$; —◇—, $\mathcal{N} = 0.96$.

geometry, the fluid between the air fingers extends far from the interface and provides a pictorial history of the location of fingers and tip splitting at the interface. At low and moderate capillary numbers, the surface would only tip-split and evolve until a stable wavenumber was reached, leading ultimately to long straight liquid bridges, whereas at high capillary numbers the interface was relatively dynamic with significant tip splitting even during fully developed flow (figure 10a) leading to oscillations in the positions of the liquid bridges where merging bridges would appear as small branches off the main bridge.

For fingering instabilities in elastic fluids, the occurrence of tip splitting was significantly enhanced as the capillary number was increased past the critical condition forming almost dendritic patterns. Instead of the occasional tip splitting seen in the Newtonian case, the fingers in the elastic fluid were constantly tip splitting resulting in liquid bridges which produced tree-like structures. The increased tip splitting at high capillary numbers was apparent even in the weakly elastic fluid $\mathcal{N} = 0.29$ (figure 10b) where the onset of the instability is virtually identical to the Newtonian fluid (figures 6, 9). For the more highly elastic fluids, the shape of the fingers at the interface changed dramatically with triangular shaped structures instead of the flattened interface associated with the Newtonian instability (figure 10c).

4. Eccentric cylinder roll-and-plate flow

Fingering instabilities in the roll-and-plate geometry (figure 2b) have been thoroughly investigated for Newtonian fluids at onset and for moderate supercritical capillary numbers by other researchers (Sullivan & Middleman 1979; Bauman *et al.* 1982; Rabaud *et al.* 1990; deBruyn & Pan 1995). For comparison, we bench-marked the behaviour of our Newtonian fluid from low to high capillary numbers. Since
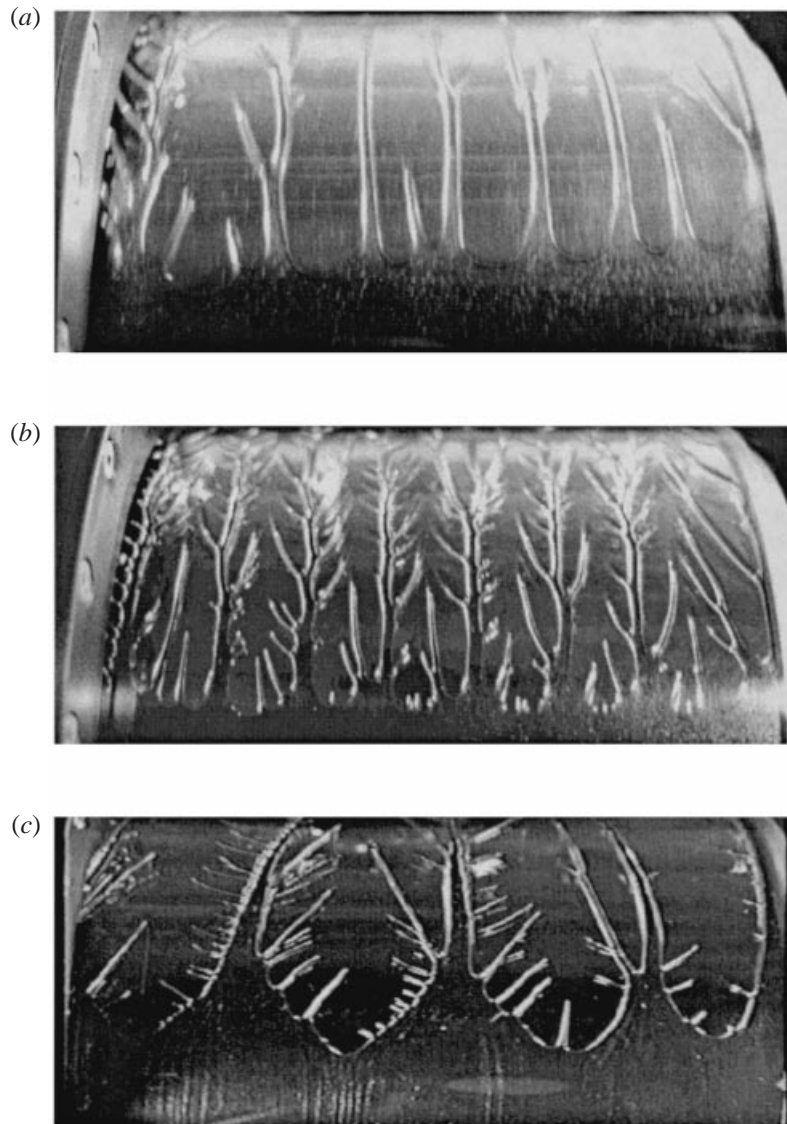
FIGURE 10. Eccentric cylinder forward roll coating instabilities for high capillary numbers ($b/R = 0.0125$): (*a*) Newtonian fluid $Ca = 4.5$; (*b*) elastic fluid $Ca = 4.4$, $\mathcal{N} = 0.29$; (*c*) elastic fluid $Ca = 5$, $\mathcal{N} = 0.96$.

gravity stabilization is important for our geometry the measured critical conditions are not comparable to those measured by other researchers. At low capillary numbers, the interface was smooth and uniform. When a critical speed was exceeded for small and moderate gap widths ($b/R \leqslant 0.075$), small undulations appeared in the interface which would then grow into the characteristic fingers associated with this class of viscous interfacial instabilities (Sullivan & Middleman 1979). The critical capillary numbers for the Newtonian fluid, as shown in figure 11, increased dramatically with gap width. For our largest gap widths ($b/R > 0.075$) we were not able to determine the Newtonian critical condition because large bubbles were drawn into the fluid from the backside of the cylinders, disrupting the coating meniscus. Previous
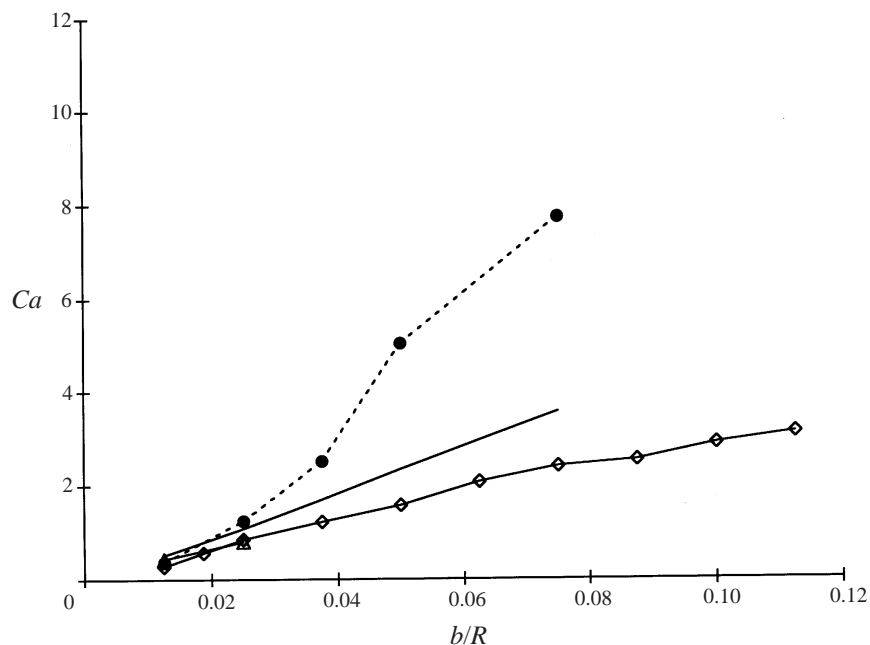
FIGURE 11. Comparison of the critical capillary number in roll-and-plate geometry versus the dimensionless gap ratio from the experimental measurements for a range of elastic fluids: - -●- -, Newtonian fluid; ——, Saffman–Taylor theory; —△—, $\mathcal{N} = 0.29$ elastic fluid; —□—, $\mathcal{N} = 0.96$ elastic fluid.

researchers have compared their results to theoretical predictions for the forward roll coating geometry since no theory exists for the roll-and-plate geometry. However, we found that the modified Saffman–Taylor theory developed for forward roll coating flow underpredicted the critical capillary number for even moderate gap widths (cf. figure 11).

As the capillary number was increased above the critical value for the Newtonian fluid, the initially thick fingers became more slender and the wavelength decreased (figure 12*a, b*). Tip splitting occurred during start-up until the correct wavelength was selected by the system. As before, once the desired wavelength was reached, there was only very occasional tip splitting at the interface. An interesting transition occurred for high capillary numbers ($Ca \gtrsim 15$). The thin liquid bridges stretching between the inner and outer cylinders separating the air fingers became so thin that they broke, forming fingerless waves at the interface instead of the traditional finger shaped interface pattern (figure 12*c*). This state was stationary, but not entirely stable, as occasionally small bridges would reach out from the tips of the waves, then snap again breaking the connection between the cylinder walls. Since the variation in location of the interface was smaller than with normal viscous fingers, the variations in surface coating thickness (by visual observation) are also smaller, resulting in a more even coating. The capillary number as a function of the observed dimensionless wavenumber is plotted in figure 13 showing a simple exponential dependence for Newtonian fluids over the whole range of capillary numbers investigated. If we more closely examine the frequency components of the wavenumber for the images shown in figure 12, we find that the wavenumber of the primary peak increases as the capillary number increases (figure 14). In all cases, at least one harmonic
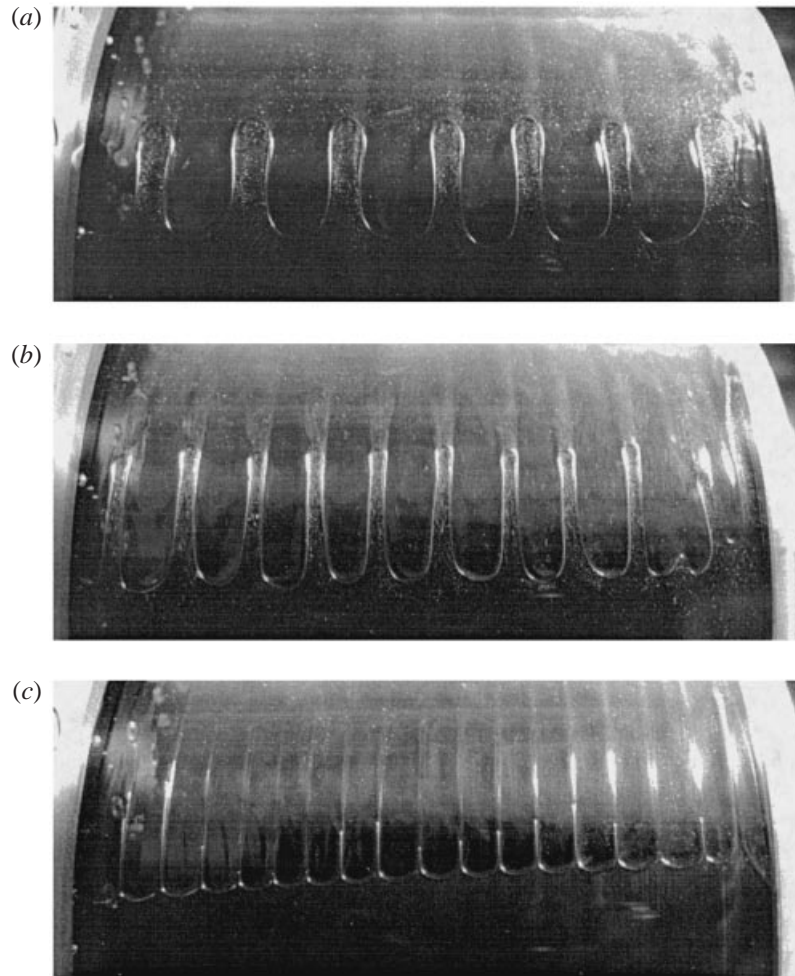
FIGURE 12. Interface patterns characteristic of various regimes of Newtonian roll-and-plate fingering instabilities ($b/R = 0.0125$): (*a*) thick fingers near critical $Ca \approx 0.8$; (*b*) thin fingers above critical $Ca \approx 2.2$; (*c*) fingerless waves $Ca \approx 61$.

peak is also captured since the interface pattern is not perfectly sinusoidal. The small deviations in the frequencies from exact harmonics are within the discretization errors of the calculation. The intensity of the primary frequency increases with the observed increase in the finger amplitude, then plummets with the appearance of the fingerless waves. The wavenumber of the primary peak agrees very well with the observed wavenumbers as shown in figure 13.

The roll-and-plate fingering instability for weakly elastic Boger fluids ($\mathcal{N} < 0.3$) appeared very similar to the Newtonian fluids for small gaps and capillary numbers ($Ca \leqslant 2$) (figures 12*a*, 15*a*). At onset, smooth fingers formed at virtually the same critical capillary number and wavenumber. The wavenumber development as capillary number increased was similar, though instead of sporadic tip splitting until a stable pattern was reached, the interface began to tip-split much more frequently until the surface was constantly tip splitting. As shown in figure 15(*b*), the interface would select a dominant wavelength which remained constant as shown by the large
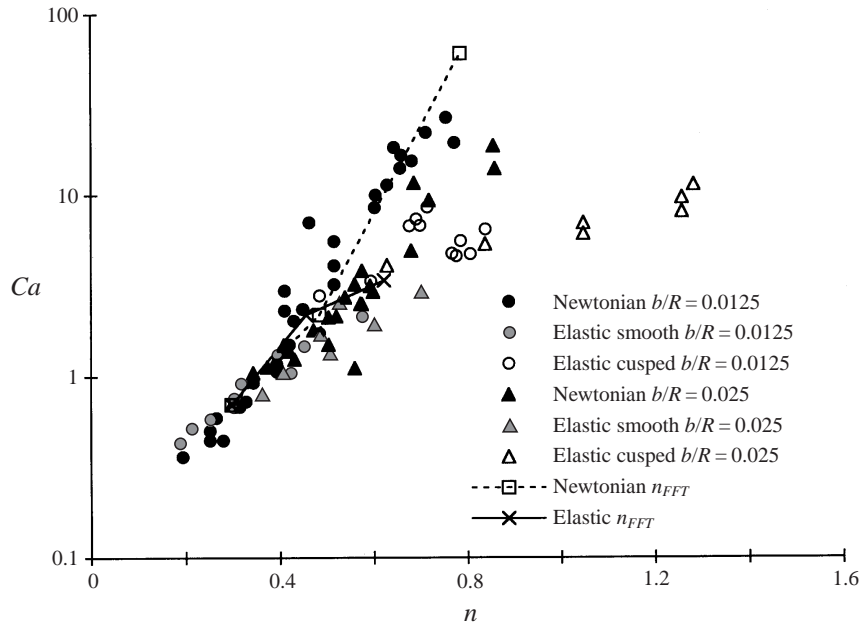
FIGURE 13. Capillary number versus wavenumber for roll-and-plate instability for two gap widths: closed symbols, Newtonian; grey symbols, elastic, smooth or chaotic interface; open symbols, elastic cusped, saw-toothed interface; - -□- -, Newtonian n_{FFT}; —×—, Elastic n_{FFT}.

liquid bridges, but the interface was very dynamic, constantly splitting and forming smaller bridges which would then merge with the larger dominant liquid bridges. For most cases a dominant observed wavenumber could be determined. These branching interface patterns did not stabilize even after over an hour of fully developed flow when at a similar value of the capillary number a Newtonian fluid interface would have stabilized in around 20 minutes. In this branched regime, the larger dominant observed wavenumber was similar to that characterizing the Newtonian viscous instability (figure 13).

Upon increasing the capillary number further, a completely different cusped, saw-toothed pattern appeared (figure 15c). When the flow was started from rest at a speed above the critical speed for 'cusping', the interface would develop similarly to the branched interface, but after a few minutes, the smooth air fingers underwent a sudden transition to a sharp pointed interface. Each finger transitioned independently. However, after a few minutes, all fingers were cusped. Close inspection of the interface as the capillary number approaches the transition reveals that the air finger was pressed very close to the stationary outer cylinder. The cusp began as a small triangle in the interface at the bottom edge of the smooth finger which would grow absorbing the entire finger. The cusped finger penetrated further into the fluid than the smooth finger had previously. For different gaps, the transition to cusped, saw-toothed fingers was not governed by the capillary number nor the Weissenberg number as shown in figure 16 leading us to speculate that the cusping transition is a complex function of both interfacial and elastic forces. For the three fluids tested, the critical conditions collapse for a scaling of $Wi^{1/2} Ca$ (figure 16c). Also, the wavenumber of the cusped fingers was characterized by a different power-law exponent than the smooth finger instabilities, increasing more quickly with increasing capillary number (figure 13 open
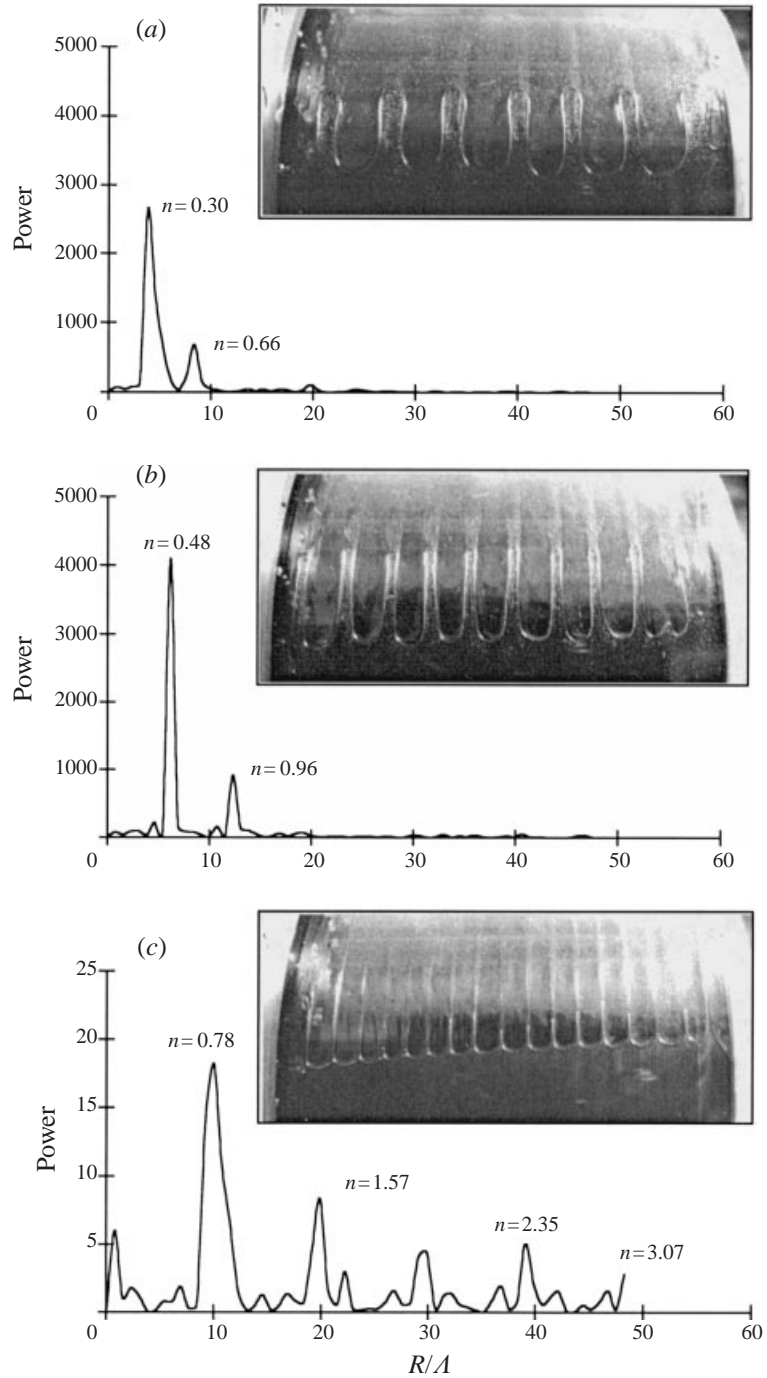
FIGURE 14. Fast Fourier transform power spectra for roll-and-plate fingering instability in Newtonian fluids for images in figure 12 ($b/R = 0.0125$): (*a*) $Ca \approx 0.8$; (*b*) $Ca \approx 2.2$; (*c*) $Ca \approx 61$.
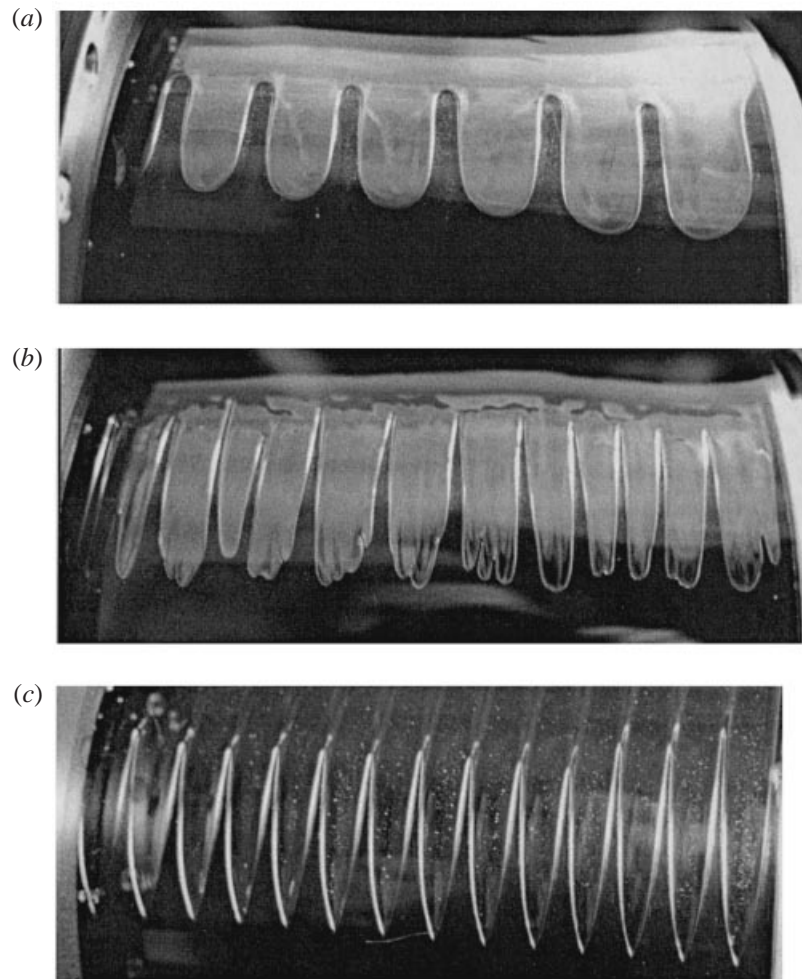
FIGURE 15. Interface patterns characteristic of various regimes of elastic roll-and-plate fingering instabilities in small gap ratios ($b/R = 0.0125$, $\mathcal{N} = 0.29$): (*a*) Thick fingers near critical $Ca = 0.7$; (*b*) chaotic behaviour above critical $Ca = 2.2$; (*c*) saw-toothed cusped fingers $Ca = 3.4$.

symbols). Note that inertially driven saw-tooth cusped instabilities have been reported previously at the free surface between air and Newtonian liquid for flow in a partially filled rotating cylinder by Thoroddsen & Mahadevan (1997).

The dynamics of the saw-toothed cusped interface were also different from the dynamics of the smooth fingers. Though they did merge with neighbouring fingers, the structure was very resistant to tip-splitting because of the pointed ends. Near the onset of cusping, the most common mechanism for surface evolution involved the cusps blunting into rounded fingers which receded away from the minimum gap, split into two fingers as shown in figure 17. The mica speck to the right of the cusped tip in the images is stationary, emphasizing the retreat of the cusped finger when it splits. Typically one of these new smooth fingers (in this case the left one) would form a cusped point and penetrate into the channel again while the other would be absorbed by its neighbour shifting the neighbouring peak to the left and decreasing the original wavelength.
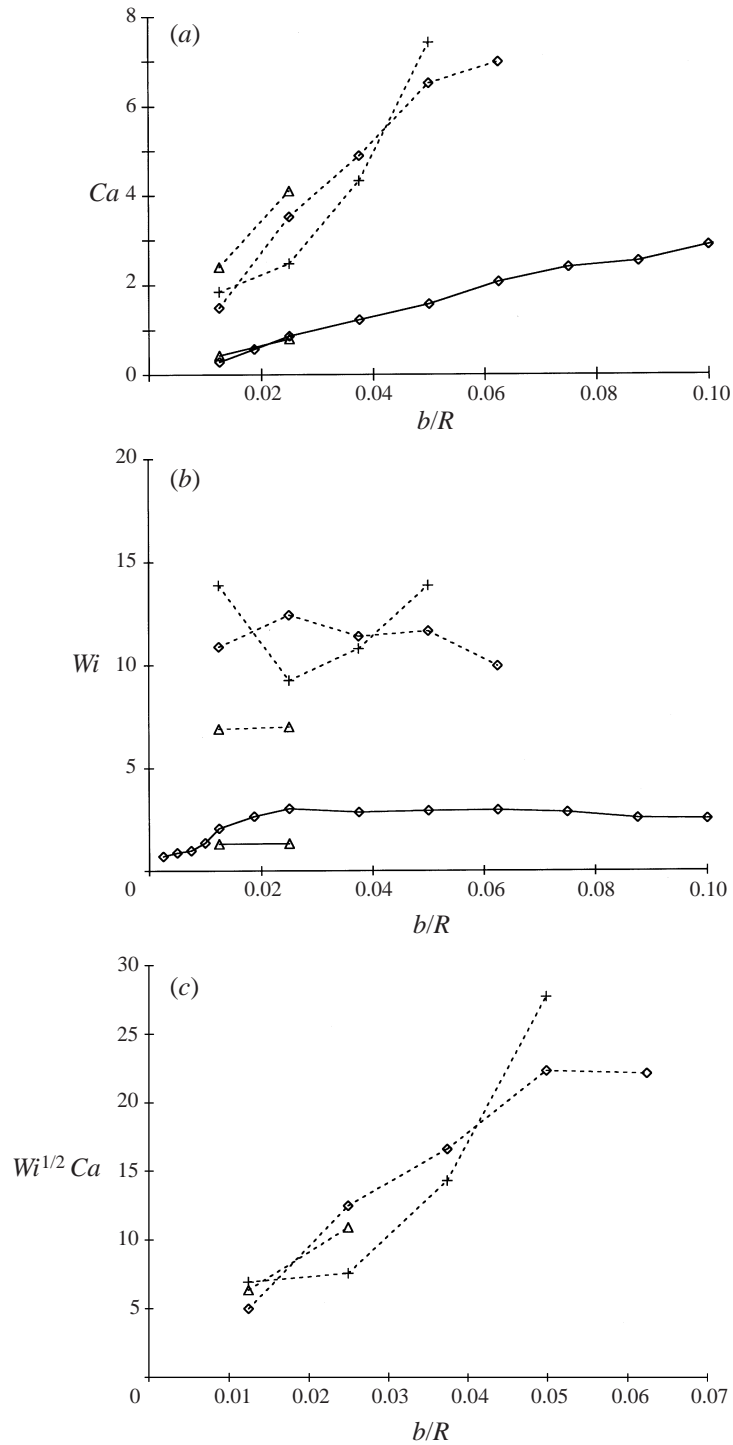
FIGURE 16. Critical condition for transition to cusped, saw-toothed fingers versus dimensionless gap ratio: (*a*) critical capillary number; (*b*) critical Weissenberg number; (*c*) $Wi^{1/2} Ca$ scaling for cusping transition: —△—, fingering critical $\mathcal{N} = 0.29$; - -△- -, cusping critical $\mathcal{N} = 0.29$; —+—, fingering critical $\mathcal{N} = 0.76$; - -+- -, cusping critical $\mathcal{N} = 0.76$; —◇—, fingering critical $\mathcal{N} = 0.96$; - -◇- -, cusping critical $\mathcal{N} = 0.96$.
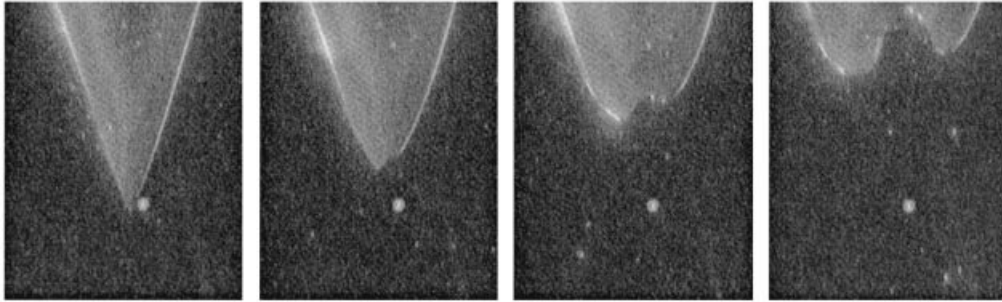
FIGURE 17. Cusp evolution through tip-splitting ($b/R = 0.0125, Ca = 5.4, \mathcal{N} = 0.29$): (*a*) $t = 0$, initial sharp cusp; (*b*) $t = 3$ s; (*c*) $t = 4.5$ s; (*d*) $t = 6$ s, two smooth round air fingers. The white mica flake to the right of the cusp in frame (*a*) is stationary.

This transition from smooth to cusped fingers can be more fully understood by looking at the Fourier analysis of the interface patterns (figure 18). For low capillary numbers, the power spectrum of the elastic interface is similar to that of the Newtonian fluid showing a primary peak at $n_{FFT} = 0.30$. As the rotation speed is increased and the interface becomes more 'dynamic', the primary frequency shifts as seen in the Newtonian spectra, but also a new frequency $n_{FFT} = 0.72$ begins to appear. During the analysis of this image, there were a few instances where the interface position was multivalued because of the splitting near the tips of the air fingers. For these cases, the lower interface position was used for the Fourier analysis. When the interface transitions to the saw-toothed cusped interface pattern, the only wavenumber apparent in the Fourier analysis is $n_{FFT} = 0.62$ with the much smaller second harmonic at $n_{FFT} = 1.31$ cm. We can now recognize the 'dynamic' interface as a transition from the initial Newtonian frequency to the elastic wavelength. A more detailed Fourier analysis of the capillary number dependence of the wavenumber is underway to help clarify the behavior as a function of gap width and fluid elasticity $\mathcal{N}$.

The conditions necessary for cusping are not well understood. Experimentally, we observed a stagnation line at the interface where the fluid splits to move around the air finger. Other researchers have postulated that a recirculation region exists near the stationary cylinder at the meniscus (Bauman *et al.* (1982), Sullivan & Middleman (1979)) similar to those seen in forward roll coating flow by Pitts and Greiller (1961). The resulting stagnation point flow near the outer cylinder is similar to the cusping flows studied by Jeong & Moffatt (1992). Joseph, Nelson, Renardy & Renardy (1991) found that elastic fluids formed cusps at capillary numbers smaller than those characterizing Newtonian fluids, but this can not explain why only the elastic fluids display cusped interfaces. Even at capillary numbers five times the critical value for cusping in an elastic fluid, the Newtonian fluid showed no signs of this transition. It is possible that other changes in the flow associated with the formation of the fingerless waves precludes the formation of cusps. It is also possible that the presence of elasticity causes a change in the flow near the meniscus which is necessary for the cusping behaviour. Mackley (1978) and Farrell & Keller (1978) found that the localized high extensional viscosity of polymers near stagnation points produces a reduction in the local strain rate and modifies the velocity field in asymmetric flows such as this one. We can only speculate as to how this might affect such a complex two dimensional flow.
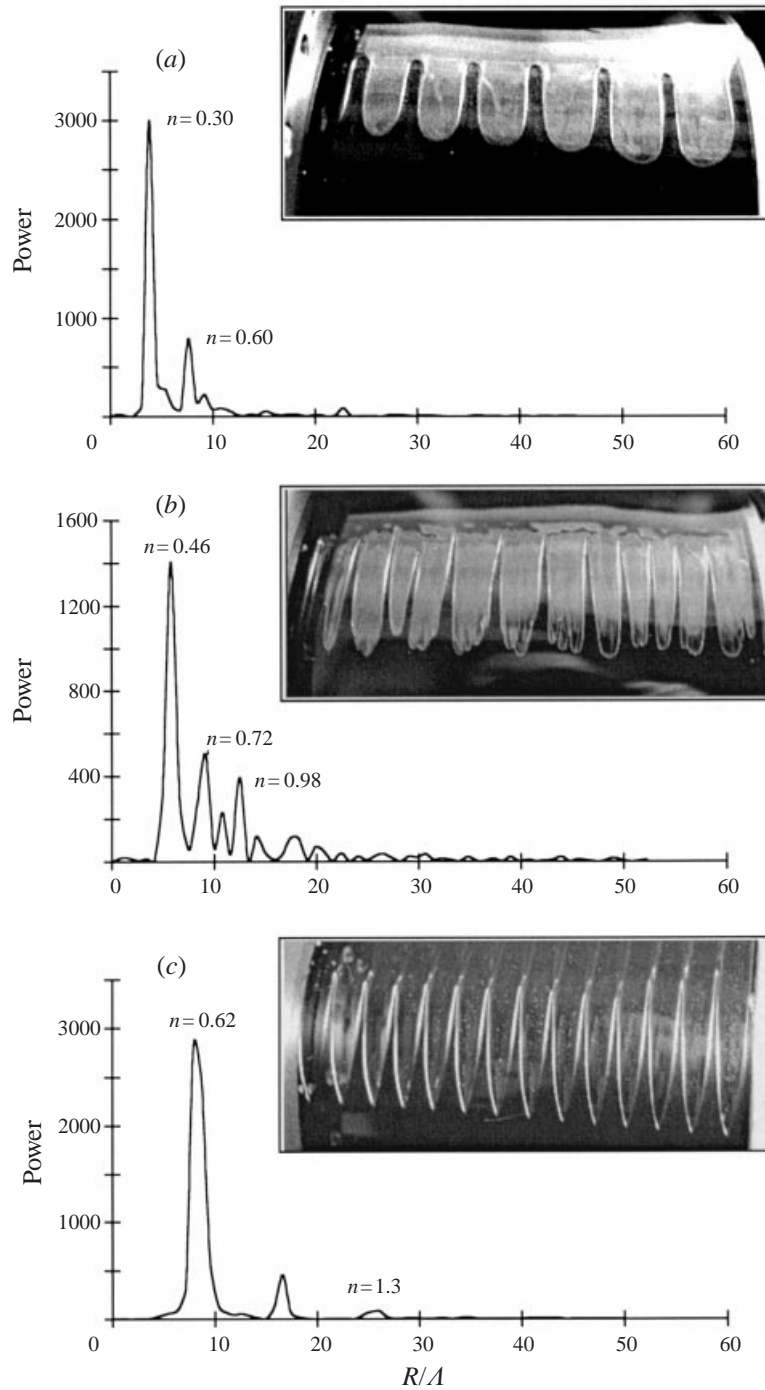
FIGURE 18. Fast Fourier transform power spectra for roll-and-plate fingering instability in elastic fluids for images in figure 15 ($b/R = 0.0125$, $\mathcal{N} = 0.29$): (a) $Ca = 0.7$; (b) $Ca = 2.2$; (c) $Ca = 3.4$.

Another possible explanation is that the smooth round fingers are elastically unstable. The flow around the rounded tips of the smooth fingers creates hoop stresses which act to squeeze around the air finger. As the Weissenberg number is increased these stresses could become large enough to make the tip of the air finger collapse. The interface pattern chosen by the system, the pointed tip, has a more gradual splitting of the fluid which would result in smaller hoop stresses.

5. Inverse roll-and-plate flow

The next flow that we studied was the inverse roll-and-plate flow shown in figure 2(c). Because our experimental fluids have high viscosities, it was necessary to place a block between the cylinders to keep the fluid at the bottom of the apparatus. Given this configuration, the more viscous fluid is displacing air; thus, for Newtonian fluids this flow is stable to viscous fingering instabilities. Indeed, our experiments with Newtonian fluids confirmed that the interface is stable at very high rotation speeds (Newtonian flow is stable at $U = 4$ cm s^{-1} whereas the critical speed for interface deformation in an elastic fluid of $\mathcal{N} = 0.19$ is $U = 1.7$ cm s^{-1}). There is however a purely elastic instability associated with the recirculation region near the block which has a critical Weissenberg number, $Wi_c \approx 2$ (Grillet & Shaqfeh 1996).

At low speeds, corresponding to low capillary and Weissenberg numbers, the flow of the elastic fluid is stable with a smooth interface. Above the critical condition for the recirculation instability, a banded pattern appeared in the mica flakes in the fluid near the block. Near the critical Weissenberg number, the instability was localized near the block and the interface was still smooth and stable. As the Weissenberg number increased above critical, the instability strengthened and the mica flake patterns began to propagate throughout the flow. As the flow was further strengthened, the mica flake patterns appeared not only in the bulk fluid, but also in the recirculation region near the interface (figure 19a). We are certain that these patterns are associated not with a new instability, but with the previously documented instability near the block (Grillet & Shaqfeh 1996).

Above a critical Weissenberg number, approximately twice that necessary for the purely elastic instability near the block, surface deformations began to appear in the air–fluid interface. Near onset, the deformations were smooth and regular, but did not resemble the viscous fingers discussed previously (figure 19b,c). These deformations were correlated with the mica flake patterns caused by the recirculation instability and had the same wavenumber as the recirculation instability near the block (figure 19d). We believe that they were caused by that instability. As the Weissenberg number increased, the recirculation instability strengthened such that the associated vortices penetrated further into the bulk flow. The surface deformations appeared when the bulk flow vortices attained sufficient strength to propagate to the other side of the apparatus and deform the surface. When the Weissenberg number increased further, 'tip splitting' was more frequent and the interface between the fluid fingers was drawn into traditional cusped shapes similar to those seen by Joseph *et al.* (1991).

6. Inverse forward roll coating flow

The last geometry studied is inverse forward roll coating flow between concentric cylinders (figure 2d). This flow is equivalent to that near the interface during the pumping of an elastic fluid into a channel, as in injection moulding of molten plastics. For Newtonian fluids, we confirmed that the interface was again stable. Because of
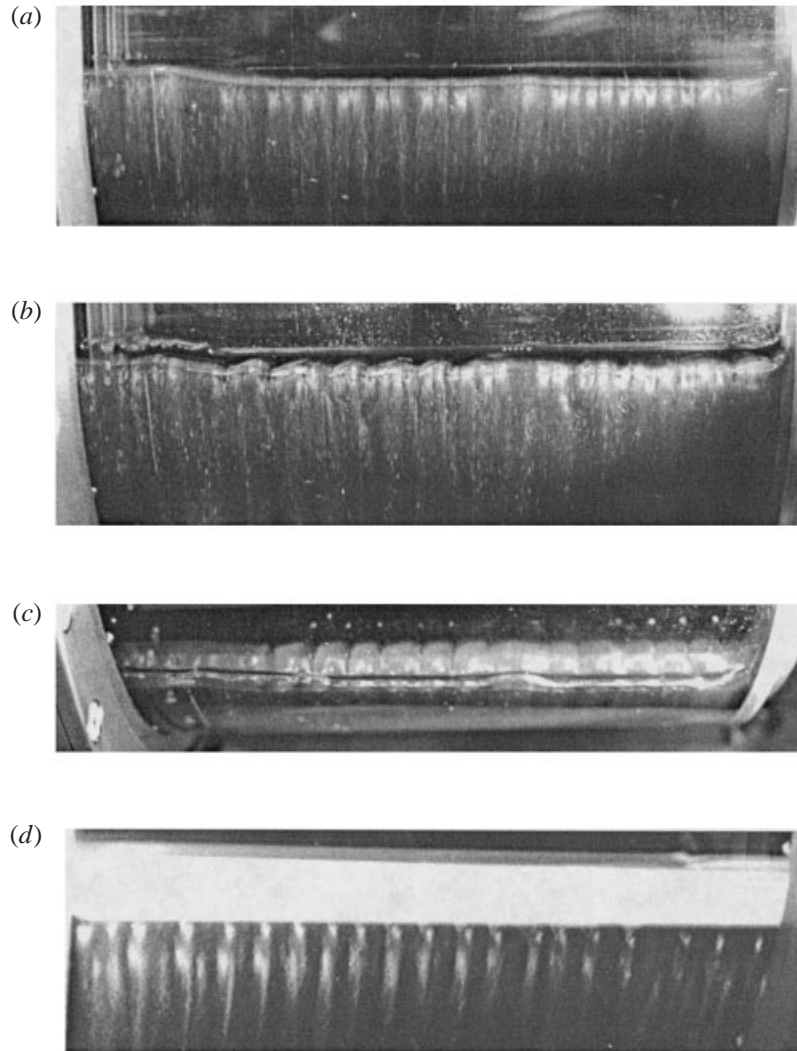
FIGURE 19. Inverse roll-and-plate flow instabilities: (*a*) mica patterns with smooth interface $Wi = 3.6$; (*b*) interface deformations with mica patterns $Wi = 4.0$; (*c*) top view of interface deformations $Wi = 4.0$; (*d*) purely elastic instability at the block.

the presence of the block, there was also a purely elastic instability associated with the flow near the block (Grillet & Shaqfeh 1996).

For flows of Boger fluids at low speeds ($Wi < 2$), the interface was stable forming a rounded almost semi-circular surface with a stagnation point in the middle of the channel. The recirculation region near the block became unstable at $Wi = 2$ (Grillet & Shaqfeh 1996). Even as the velocities were increased above critical, no mica flake patterns were visible at the air–fluid interface. If the secondary flow due to the instability at the block was not strong enough to produce a visible secondary flow, it appears reasonable that the flow in the region around the air–fluid interface was not affected.

Above a critical Weissenberg number $Wi_c \approx 2.4$ ($\mathcal{N} = 0.19$), we observed deformations in the air–fluid interface. At this Weissenberg number, these deformations
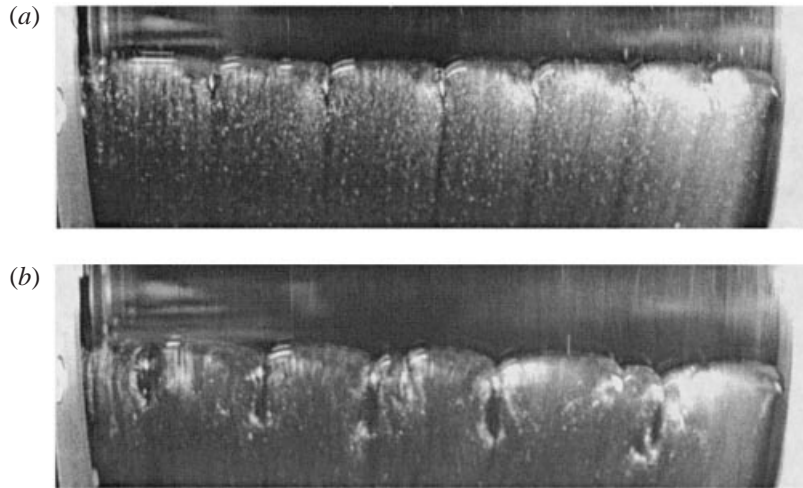
FIGURE 20. Inverse forward roll coating flow: cusped surface deformations: (*a*) near critical $Wi = 2.4$; (*b*) above critical with tip-splitting at two centre-right fingers $Wi = 6.0$.

appeared as smooth sinusoidal variations, but quickly developed into sharp cusps pointing into the fluid (figure 20*a*). The mica flakes in the fluid leaving the cusped interface region showed a banded pattern indicative of an instability with vortices propagating into the fluid. Near the interface, these vortices would create a flow similar to the flow used by Joseph *et al.* (1991) to study cusp formation. The wavenumber of the instability was approximately $n = 3$, much smaller than the wavenumber associated with the purely elastic instability near the block ($n = 16$), providing additional evidence that the two instabilities are not coupled. Above the critical condition, the inverse forward roll coating flow instability appeared immediately at startup of the flow, suggesting that it originated at the air–fluid interface. Additionally, the interface pattern was dynamic with new cusps splitting and merging continuously (figure 20*b*).

7. Summary

Our study of several fluid displacement flows with the goal of understanding the role of elasticity in the stability of interfaces has revealed previously unknown surface dynamics. The onset of traditional Newtonian viscous fingering in eccentric cylinder forward roll coating flow was found to be controlled by gravity stabilization for all but the smallest gap widths investigated and was well predicted by a modified Saffman–Taylor theory. As the speed was increased above the critical condition, the wavenumber n of the instability increased, and the primary wavenumber from a Fourier analysis of the interface confirmed the location of the primary peak had shifted. We find that the effect of elasticity in these flows can be correlated by using the elasticity parameter $\mathcal{N} = \lambda\sigma/\mu b_{max}$. Weakly elastic fluids ($\mathcal{N} \leqslant 0.3$) had virtually identical critical conditions and wavenumbers as the Newtonian fluid for all gap widths. However, highly elastic fluids ($\mathcal{N} \geqslant 0.5$) displayed strong destabilization in the critical gravity parameter or capillary number as well as a pronounced increase in the dimensionless wavenumber. All elastic fluids displayed increased tip-splitting above critical with the highly elastic fluids having more triangular interface shapes.

Viscous fingering instabilities were also studied in the eccentric-cylinder roll-and-plate flow. As in the forward roll coating geometry, our critical capillary numbers were larger than those observed by other researchers owing to gravity stabilization. There has been no theory derived for the Newtonian flow in this geometry, and this stabilization cannot be explained by using the modified Saffman–Taylor theory for forward roll coating flow. The observed and Fourier wavenumbers were both found to increase with capillary number above the critical condition. At very high capillary numbers, a novel fingerless wave interface pattern was documented. Because the amplitude of these peaks was smaller, the resulting variations in the thickness of the coating film were reduced.

We have also discovered novel interface patterns associated with fingering instabilities of elastic fluids in the roll-and-plate geometry. The capillary numbers at onset of instability for highly elastic fluids were again significantly lower than those characterizing Newtonian fluids by up to a factor of 4. Significantly above the critical condition, all fluids underwent a transition to a saw-toothed, cusped interface pattern. The critical condition for this cusping transition was not directly dependent on capillary number nor Weissenberg number, but rather scales with $Wi^{1/2}\,Ca$ for the range of elastic fluids examined. We believe the cusping is caused by a combination of the high polymer extensional viscosities near the interface stagnation points and the backflow region near the stationary outer cylinder.

We have also looked at several flows which are stable to traditional fingering instabilities where the more viscous fluid displaces the less viscous fluid (fluid$\Rightarrow$air displacement flows). Investigating the inverse roll-and-plate flow we demonstrated that purely elastic instabilities in the bulk flow can cause surface deformations at the fluid–air interface. Recirculation flows are prevalent in polymer processing applications, including the fluid pool behind a blade coater, and the contraction flow upstream of extrusion dies (Aidun *et al.* 1991; Kraynik & Schowalter 1981). Our results suggest that elastic instabilities in the upstream recirculation flows could affect the nearby free surfaces if the secondary flow was of sufficient strength. In inverse forward roll coating flow, we discovered a new class of purely elastic instabilities which are independent of viscous fingering instabilities and bulk flow elastic instabilities. Given that inverse roll coating flow is similar to pressure-driven injection moulding into a channel, elastic instabilities at the interface could cause defects in the final moulded product because of quenched elastic stresses, entrained air, polymer degradation or inherent weak regions in the plastic.

Interfacial flows of elastic fluids show a wide range of dynamics, more diverse than suggested by previous work. Dramatic changes in traditional viscous fingering occur in elastic fluids, including a new class of purely elastic instabilities at the interface. Highly elastic fluids have been shown to strongly reduce the critical flow rates and decrease the onset wavelength of the fingering instability. We look forward to continued exploration of elastic interfacial flows, and we seek to address many of the questions we have raised in future work.
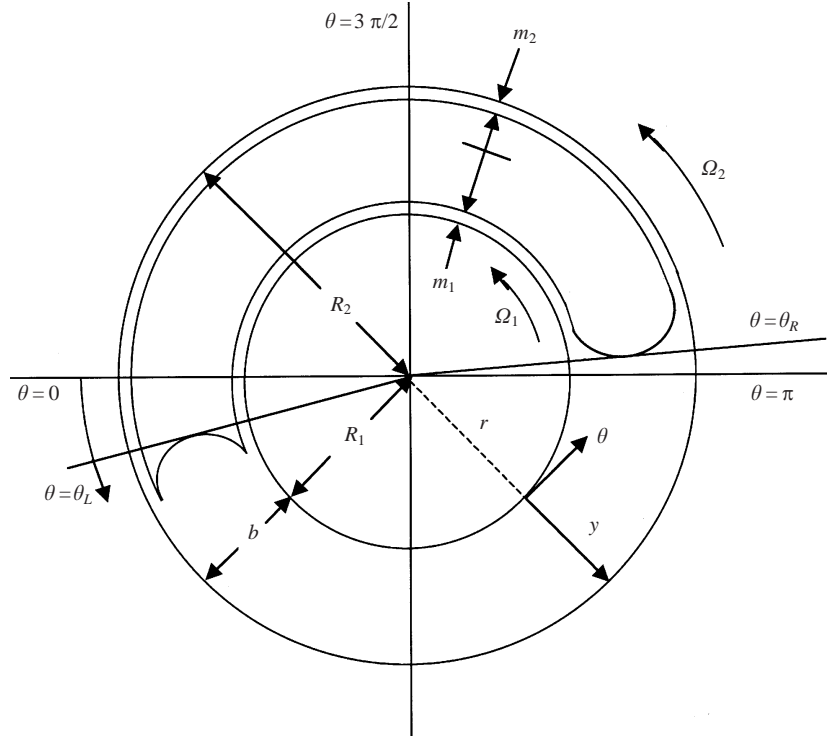
FIGURE 21. Sketch of the coordinate system on the two rotating cylinders.

Appendix. The linear stability equations for concentric cylinder coating flows with finite film thickness

In this Appendix, the linear stability equations and results for concentric cylinder coating flows with finite film thickness are developed. The equations valid in the region away from the interface (cf. figure 21) are non-dimensionalized by using the radius of the inner cylinder, R_1, as the appropriate lengthscale. The origin of the cylindrical coordinate $(\bar{r}, \theta, \bar{z})$ is located at the centre of the smaller cylinder (cf. figure 21); the $\bar{z}$-coordinate is parallel to the axes of the cylinders and the local $\bar{y}$-coordinate is related to $\bar{r}$ by $\bar{y} = (\bar{r} - 1)/\delta$, where $\delta = b/R_1$ and b is the gap thickness (cf. figure 21). Neglecting terms of $O(\delta) = O(b/R_1)$, the usual lubrication approximation to Cauchy's equations of motion along with the corresponding continuity equation are obtained:

$$0 = -\frac{\partial \bar{p}}{\partial \theta} + \frac{\partial^2 \bar{v}_\theta}{\partial \bar{y}^2} - \frac{\cos \theta}{G}, \tag{A 1}$$

$$0 = \frac{\partial \bar{p}}{\partial \bar{y}}, \tag{A 2}$$

$$0 = -\frac{\partial \bar{p}}{\partial \bar{z}} + \frac{\partial^2 \bar{v}_z}{\partial \bar{y}^2}, \tag{A 3}$$

$$0 = \frac{\partial \bar{v}_\theta}{\partial \theta} + \frac{\partial \bar{v}_z}{\partial \bar{z}}, \tag{A 4}$$

where $\bar{v}_\theta$ and $\bar{v}_z$ are the azimuthal and longitudinal velocities made dimensionless with the rotation speed of the inner cylinder, $\Omega_1 R_1$, and are subject to the usual no-slip

boundary conditions

$$\bar{v}_\theta = 1, \ \bar{v}_z = 0 \quad \text{on} \quad \bar{y} = 0, 1. \tag{A 5}$$

As defined in the body of the text (cf. (1.2)), $G = \mu\Omega_1 (R_1 + R_2)/2b^2\rho g$. There are two interface conditions. The gap-averaged kinematic condition (Reinelt 1995) is given by

$$\langle \bar{v}_\theta \rangle \, |_{\theta_j} = \bar{m}_1 + \bar{m}_2, \tag{A 6}$$

where the variables enclosed by angled brackets in (A 6) are gap averaged. $\theta_j = \theta_L, \theta_R$ refers to the left and right interfaces, and $\bar{m}_1$ and $\bar{m}_2$ are the film thicknesses made dimensionless with the gap, b (cf. figure 21). A momentum balance performed on the thin film region shows that the gravity force gives rise to a θ-dependent term of $O\left(\bar{m}_{1,2}^3\right)$ which is neglected in our derivations because we assumed $\bar{m}_{1,2} \ll 1$; therefore, $\bar{m}_1$ and $\bar{m}_2$ become constants. We found this to be true in our experiments a few gap thicknesses away from the interface. The film thickness measurements were ultimately made at $\theta = 3\pi/2$ (cf. figure 21) to completely eliminate the effect of gravity and hence the variation of the film thickness. The surface tension terms near the meniscus are of $O(\delta^2)$ so the pressure jump condition at $\theta = \theta_L$ and $\theta = \theta_R$ is approximated as

$$\bar{p}|_{\theta_j} = 0. \tag{A 7}$$

The formulation of the problem is completed by requiring that the total amount of fluid be conserved. Let $\bar{V}_o$ be the volume of fluid confined between the two cylinders non-dimensionalized with bR_1^2. Again neglecting terms of $O(\delta)$, we have

$$\bar{V}_o = \int_0^{L/R_1} [(\theta_R - \theta_L) + (2\pi - (\theta_R - \theta_L))(\bar{m}_1 + \bar{m}_2)] \, \mathrm{d}\bar{z}. \tag{A 8}$$

This condition is necessary to determine the relative position of the two interfaces where the boundary conditions must be applied. When the gap between the cylinders is initially half-filled,

$$\theta_R - \theta_L = \frac{\pi(1 - 2(\bar{m}_1 + \bar{m}_2))}{1 - \bar{m}_1 - \bar{m}_2}. \tag{A 9}$$

Solving these equations and assuming $\bar{m}_1 = \bar{m}_2 = \bar{m}$ the following steady-state solutions are obtained:

$$\bar{v}_\theta^o = 6(1 - 2\bar{m})(\bar{y}^2 - \bar{y}) + 1, \tag{A 10}$$

$$\bar{p}^o = -\frac{\sin(\theta)}{G} + \frac{\sin(\theta_R)}{G} + 12(1 - 2\bar{m})(\theta - \theta_R), \tag{A 11}$$

$$\frac{\sin(\theta_R)}{G} - \frac{\sin(\theta_L)}{G} = 12\pi(1 - 4\bar{m}), \tag{A 12}$$

$$\theta_L = \theta_R - \frac{\pi(1 - 4\bar{m})}{1 - 2\bar{m}} \approx \theta_R - \pi(1 - 2\bar{m}) + O\left(\bar{m}^2\right). \tag{A 13}$$

To analyse the stability of the interfacial flow, sinusoidal disturbances are introduced at each interface edge. The linearized equations are then solved to determine whether the amplitude of the perturbations grows or decays for different flow conditions. The perturbations are given by

$$\theta_j = \theta_j^o + \theta_j', \tag{A 14}$$

$$\theta_j' = a_j \exp\left(\mathrm{i}\tilde{n}\bar{z} + S\bar{t}\right), \tag{A 15}$$

where S is the growth rate of disturbances and $a_j \ll 1$. Note that we have only considered perturbations where the sinusoidal disturbances on the two interfaces are

'in phase', however, this does not affect our final result. In the fluid, the velocity and pressure components are given by

$$\bar{v}_\theta = \bar{v}_\theta^o + \bar{v}_\theta', \tag{A 16}$$

$$\bar{v}_z = \bar{v}_z', \tag{A 17}$$

$$\bar{p} = \bar{p}^o + \bar{p}', \tag{A 18}$$

where $\bar{v}_\theta^o$ and $\bar{p}^o$ are the steady-state solutions; the disturbance velocities are subject to the conditions

$$\bar{v}_\theta' = \bar{v}_z' = 0 \quad \text{on} \quad \bar{y} = 0, 1. \tag{A 19}$$

Using the equations of motion (1)–(3) along with the pressure jump condition at the interface,

$$\left(\bar{p}^o + \bar{p}'\right)|_{\theta_j} = 0, \tag{A 20}$$

we get

$$\bar{v}_\theta' = -\frac{1}{2}\frac{\partial \bar{p}'}{\partial \theta}\,\bar{y}\,(1-\bar{y}), \tag{A 21}$$

$$\bar{v}_z' = -\frac{1}{2}\frac{\partial \bar{p}'}{\partial \bar{z}}\,\bar{y}\,(1-\bar{y}), \tag{A 22}$$

$$\bar{p}'|_{\theta_j^o} = \left(12\,(1-2\bar{m}) - \frac{\cos(\theta_j^o)}{G}\right) a_j \exp\left(i\tilde{n}\bar{z} + S\bar{t}\right). \tag{A 23}$$

Further assuming that the disturbance pressure is of the form

$$\bar{p}' = g\,(\theta)\exp\left(i\tilde{n}\bar{z} + S\bar{t}\right), \tag{A 24}$$

where $g\,(\theta)$ is found from continuity,

$$\frac{\partial^2 \bar{p}'}{\partial \theta^2} + \frac{\partial^2 \bar{p}'}{\partial \bar{z}^2} = 0, \tag{A 25}$$

we have

$$g\,(\theta) = A\sinh\,(\tilde{n}\theta) + B\cosh\,(\tilde{n}\theta), \tag{A 26}$$

where A and B are constants of integration. The formulation of the stability problem is therefore complete. By applying the kinematic and pressure jump conditions at the interfaces, and assuming proximity to the critical point (i.e. $S \ll 1$), the following expression for the growth rate of disturbances can be derived:

$$S = \tilde{n}\tanh\,(\tilde{n}\pi\,(1-2\bar{m}))\left(1 - \frac{\cos(\theta_R)}{12G\,(1-2\bar{m})}\right). \tag{A 27}$$

If the interaction between the two interfaces were neglected (single interface perturbation) then the following expression for S (cf. (3.8)) is obtained instead:

$$S = \tilde{n}\left(1 - \frac{\cos(\theta_R)}{12G\,(1-2\bar{m})}\right). \tag{A 28}$$

Note that the critical condition ($S = 0$) is defined by

$$G = \frac{\cos(\theta_R)}{12\,(1-2\bar{m})} \tag{A 29}$$

for both (A 27) and (A 28). Equation (A 28) is consistent with equation (3.8) if we note that $S = \Gamma/Ca$ and $h = b$.

REFERENCES

AIDUN, C. K., TRIANTAFILLOPOULOS, N. G. & BENSON, J. D. 1991 Global stability of a lid-driven cavity with throughflow: Flow visualization studies. *Phys. Fluids* A **3**, 2081–2091.

ALLEN, E & BOGER, D. V. 1988 The influence of rheological properties on viscous fingering in enhanced oil recovery. *Xth Intl Congr. on Rheology* (ed. P. H. T. Uhlherr), pp. 146–148. ASR, Sydney, N.S.W.

BAUMAN, T., SULLIVAN, T. & MIDDLEMAN, S. 1982 Ribbing instability in coating flows: Effect of polymer additives. *Chem. Engng Commun.* **14**, 35–46.

BOGER, D. V. & MACKAY, M. E. 1991 Continuum and molecular interpretation of ideal elastic fluids. *J. Non-Newtonian Fluid Mech.* **41**, 133–150.

BYARS, J. A., ÖZTEKIN, A., BROWN, R. A. & MCKINLEY, G. H. 1994 Spiral instabilities in the flow of highly elastic fluids between rotating parallel disks. *J. Fluid Mech.* **271**, 173–218.

COYLE, D. J., MACOSKO, C. W. & SCRIVEN, L. E. 1990 Stability of symmetric film-splitting between counter-rotating cylinders. *J. Fluid Mech.* **216**, 437–458.

DEBRUYN, J. R. & PAN, L. 1995 Delayed onset of ribbing instability due to finite-size effects. *Phys. Fluids* **7**, 2185–2190.

DONTULA, P., PASQUALI, M., MACOSKO, C. W. & SCRIVEN, L. E. 1996 Viscoelastic effects in forward-roll coating flows. *Proc. XIIth Intl Congr. on Rheology* (ed. A. Ait-kadi). Quebec City, Canada.

DRIS, I. M. & SHAQFEH, E. S. G. 1995 On purely elastic instabilities in eccentric cylinder flows. *J. Non-Newtonian Fluid Mech.* **56**, 349–360.

FARRELL, C. J. & KELLER, A. 1978 The observation of high polymer chain extension with two counter-rotating rollers. *Colloid Polymer Sci.* **256**, 966–969.

FERNANDO, R. H. & GLASS, J. E. 1988 Dynamic uniaxial extensional viscosity (DUEV) effects in roll application: II. Polymer blend studies. *J. Rheol.* **32**, 199–213.

GREENER, J., SULLIVAN, T., TURNER, B. & MIDDLEMAN, S. 1980 Ribbing instability of a two-roll coater: Newtonian fluids. *Chem. Engng Commun.* **5**, 73–83.

GRILLET, A. M. & SHAQFEH, E. S. G. 1996 Observations of viscoelastic instabilities in recirculation flows of Boger fluids. *J. Non-Newtonian Fluid Mech.* **64**, 141–155.

HOMSY, G. M. 1987 Viscous fingering in porous media. *Ann. Rev. Fluid Mech.* **19**, 271–311.

JEONG, J.-T. & MOFFATT, H. K. 1992 Free-surface cusps associated with flow at low Reynolds number. *J. Fluid Mech.* **241**, 1–22.

JOO, Y. L. 1993 A theoretical and experimental investigation of viscoelastic instabilities in Taylor–Dean flows. PhD thesis, Stanford University.

JOO, Y. L. & SHAQFEH, E. S. G. 1991 Viscoelastic Poiseuille flow through a curved channel: A new elastic instability. *Phys. Fluids* A **3**, 1691–1694.

JOO, Y. L. & SHAQFEH, E. S. G. 1994 Observations of purely elastic instabilities in the Taylor–Dean flow of a Boger fluid. *J. Fluid Mech.* **262**, 27–73.

JOSEPH, D. D., NELSON, J., RENARDY, M. & RENARDY, Y. 1991 Two-dimensional cusped interfaces. *J. Fluid Mech.* **223** 383–409.

KRAYNIK, A. M. & SCHOWALTER, W. R. 1981 Slip at the wall and extrudate roughness with aqueous solutions of polyvinyl alcohol and sodium borate. *J. Rheol.* **25**, 95–114.

LARSON, R. G. 1988 *Constitutive Equations for Polymer Melts and Solutions.* Butterworths.

LARSON, R. G., SHAQFEH, E. S. G. & MULLER, S. J. 1990 A purely elastic instability in Taylor–Couette flow. *J. Fluid Mech.* **218**, 573–600.

MACKLEY, M. R. 1978 Flow singularities, polymer chain extension and hydrodynamic instabilities. *J. Non-Newtonian Fluid Mech.* **4**, 111–136.

MAGDA, J. J. & LARSON, R. G. 1988 A transition occurring in ideal elastic liquids during shear flow. *J. Non-Newtonian Fluid Mech.* **30**, 1–19.

MCKINLEY, G. H., PAKDEL, P. & ÖZTEKIN, A. 1996 Rheological and geometric scaling of purely elastic flow instabilities. *J. Non-Newtonian Fluid Mech.* **67**, 19–47.

MICHALLAND, S., RABAUD, M. & COUDER, Y. 1996 Instabilities of the upstream meniscus in directional viscous fingering. *J. Fluid Mech.* **312**, 125–148.

MILL, C. C. & SOUTH, G. R. 1967 Formation of ribs on rotating rollers. *J. Fluid Mech.* **28**, 523–529.

MULLER, S. J., LARSON, R. G. & SHAQFEH, E. S. G. 1989 A purely elastic transition in Taylor–Couette flow. *Rheol. Acta* **28**, 499–503.

Ning, C.-Y. , Tsai, C.-C. & Liu, T.-J. 1996 The effect of polymer additives on extrusion slot coating. *Chem. Engng Sci.* **51**, 3289–3297.

Pakdel, P., Speigelberg, S. & McKinley, G. H. 1997 Cavity flows of elastic liquids: two-dimensional flows. *Phys. Fluids* **9**, 3123–3140.

Pearson, J. R. A. 1959 The instability of uniform viscous flow under rollers and spreaders. *J. Fluid Mech.* **7**, 481–500.

Pitts, E. & Greiller, J. 1961 The flow of thin films between rollers. *J. Fluid Mech.* **11**, 33–50.

Rabaud, M., Michalland, S. & Couder, Y. 1990 Dynamical regimes of directional viscous fingering: Spatiotemporal chaos and wave propagation. *Phys. Rev. Lett.* **64**, 184–187.

Reinelt, D. A. 1995 The primary and inverse instabilities of directional viscous fingering. *J. Fluid Mech.* **285**, 303–327.

Ruschak, K. J. 1985 Coating flows. *Ann. Rev. Fluid Mech.* **17**, 65–89.

Saffman, P. G. & Taylor, G. 1958 The penetration of a fluid into a porous medium or Hele–Shaw cell containing a more viscous liquid. *Proc. R. Soc. Lond.* A **245**, 312–329.

Shaqfeh, E. S. G. 1996 Purely elastic instabilities in viscometric flows. *Ann. Rev. Fluid Mech.* **28**, 129–185.

Shaqfeh, E. S. G., Muller, S. J. & Larson, R. G. 1992 The effect of gap width and dilute solution properties on the viscoelastic Taylor–Couette instability *J. Fluid Mech.* **235**, 285–317.

Soules, D. A., Fernando, R. H. & Glass, J. E. 1988 Dynamic uniaxial extensional viscosity (DUEV) effects in roll application: I. Rib and web growth in commercial coatings. *J. Rheol.* **32**, 181–198.

Strenger, M. R., Secor, R. B. & Lenz, B. 1997 Knife coating method using ascension of the fluid by its tension. U.S. Patent 5,612,092.

Sullivan, T. M. & Middleman, S. 1979 Roll coating in the presence of a fixed constraining boundary. *Chem. Engng Commun.* **3**, 469–482.

Thoroddsen, S. T. & Mahadevan, L. 1997 Experimental study of coating flows in a partially filled horizontally rotating cylinder. *Exps. Fluids/***23**, 1–13.

Weisser, E. M. 1996 Miscible displacement in a radial Hele–Shaw cell. PhD thesis, University of Melbourne, Australia.